

1
2 **Environmental Response in Coupled Energy and Water Cloud Impact**

3 **Parameters Derived from A-Train Satellite, ERA-Interim and MERRA-2**

4 **Lu Sun^{1,5}, A.D. Rapp², T. L'Ecuyer^{2,3}, A.S. Daloz^{2,3,4} and E. Nelson^{2,6}**

5
6 ¹Department of Atmospheric Sciences, Texas A&M University, College Station, TX, USA.

7 ²Atmospheric and Oceanic Sciences Department, University of Wisconsin-Madison, Madison,
8 WI, USA.

9 ³Center for Climate Research, University of Wisconsin-Madison, Madison, WI, USA.

10 ⁴CICERO, Gaustadalléen 21, Oslo, Norway.

11 ⁵Department of Physics, University of Auckland, Auckland, New Zealand.

12 ⁶Jet Propulsion Laboratory, California Institute of Technology, Pasadena, CA, USA

13
14
15 Corresponding author: Lu Sun (lusun@tamu.edu)

16
17
18 **Key Points:**

- 19 • Coupled cloud impact parameters in reanalyses and observations have similar patterns,
20 but opposite biases in high and low cloud regimes
- 21 • Reanalyses show less (more) heating (cooling) of the atmosphere in high (low) sea
22 surface temperature and column water vapor environments
- 23 • Water vapor is a stronger control than sea surface temperature on coupled cloud impact
24 parameters, especially in reanalyses
25

26 **Abstract**

27 Understanding the connections between the latent heating from precipitation and
28 atmospheric cloud radiative effects is essential for climate models to represent the cross-scale
29 link between cloud microphysics and global energy and water cycles well. In this paper, two
30 energy and water cycle coupling cloud impact parameters (CIPs), R_c , cooling efficiencies and R_h ,
31 heating efficiencies are used to characterize how efficiently clouds can heat the
32 atmosphere or cool the surface, respectively per unit rain from A-Train observations and two
33 reanalyses. Global distributions of CIPs are highly dependent on cloud regime and reanalyses fail
34 to simulate strong R_c and R_h at high sea surface temperature (SST)/column water vapor (CWV)
35 over deep convection regions in the Indo-Pacific warm pool region, but produce stronger R_c and
36 R_h over over SST/CWV associated with shallow, warm rain systems as in eastern Pacific marine
37 stratocumulus regions. ~~Together, this indicates the possibility that the variability of the Walker~~
38 ~~circulation simulated by reanalysis is underestimated. Conditional sampling by environmental~~
39 ~~regime shows that reanalyses have more atmospheric cooling per unit latent heating at low~~
40 ~~SST/CWV associated with shallow, warm rain systems and less atmospheric heating at high~~
41 ~~SST/CWV associated with underestimates in the radiative effects of deeper, colder clouds or~~
42 ~~overestimates in the convective precipitation.~~ The dynamic regime controls the sign of R_h , while
43 the CWV appears to be the larger control on the magnitude. The magnitude of R_c is highly
44 coupled to the dynamic regime. Observations also show two thermodynamic ~~regions~~ regime of
45 strong R_c , at low SST and CWV and at high SST and CWV, only the former of which is captured
46 by the reanalyses. While the reanalyses generate fairly similar climatologies in the frequency
47 distributions of environmental states, differences in R_c and R_h between reanalyses and A-Train
48 are linked to differences in the vertical profiles of the temperature, specific humidity and vertical
49 velocity for precipitating cloud scenes.

50

51 **Plain Language Summary**

52 Accurate projection of future climate requires understanding coupled interactions
53 between clouds, precipitation, and their environment. Here we use satellite observations to
54 calculate two parameters to reveal how efficiently ~~cloudsa-cloud~~ can heat the atmosphere or cool
55 the surface per unit rain and compare to those simulated by observationally-constrained
56 reanalysis datasets. The reanalyses show similar global patterns but have weaker atmospheric
57 heating and surface cooling per unit rain in areas of deep convection and opposite effects in low
58 cloud regions. Examination of these parameters as a function of their environment shows that
59 reanalyses cool the atmosphere too much per unit rain in environments with low sea surface
60 temperatures and water vapor. In regions with high sea surface temperature and water vapor,
61 deep convection in reanalyses does not heat the atmosphere enough per unit rain. Whether clouds
62 occur in regions of large-scale ascent or descent determines whether clouds heat or cool the
63 atmosphere and how strong the clouds cool the surface, while sea surface temperature and water
64 vapor control the strength of the atmospheric heating. Both observations and reanalyses suggest
65 that water vapor is the stronger control on how much clouds heat the atmosphere per unit rain.

66

67 **1. Introduction**

68 The role of clouds in climate ~~feedbackforcing~~, which highly depends on cloud macro-
69 and micro- physical properties, remains one of the largest uncertainties in current climate
70 projection (Bony and Dufresne 2005; Randall et al. 2007; Dessler, 2010; Choi et al. 2014 Bony
71 et al. 2015; Ceppi et al. 2017). The macro- and microphysical properties impact both cloud
72 radiative effects and the precipitation intensity of the clouds (Mace et al. 2017; Wood et al.
73 2012). To predict cloud feedbacks accurately in the climate system, two elements should be

Formatted: Line spacing: Double

74 further understood: the ability of climate models and physical parameterizations to produce cloud
75 and precipitation from changing atmospheric states and the ability to use these cloud properties
76 to estimate the radiative energy fluxes that, in turn, heat the atmosphere or cool the surface (Xu
77 et al. 2005; 2016).

78 Thus, cloud radiative effects and cloud feedback are highly connected to the precipitation
79 process and the efficiencies in converting cloud condensate to surface precipitation (Stevens and
80 Bony 2013; Bony et al. 2015). These links between the water and energy cycles occur across a
81 variety of spatial and temporal scales. At global, annual mean timescales energy constrains
82 precipitation, with precipitation increases primarily constrained by atmospheric radiative cooling
83 (Held and Soden 2006; Stephens and Ellis 2008; O’Gorman, P.A. et al. 2012; Pendergrass and
84 Hartmann 2014; Dinh and Fueglistaler 2017). Because the cloud radiative influence on the
85 exchange of radiative fluxes between the atmosphere and surface are intimately linked with the
86 water cycle through radiative-convective equilibriumbalance, the strength and location of cloud
87 radiative effects and precipitation intensity is not independent and their relative magnitudes in
88 global models depend strongly on the way clouds and convection are parameterized. The
89 coupling of radiation-precipitation occurs across scales ranging from those of climatic scale
90 (Allan et al. 2009; Previdi et al. 2010; Andrew et al. 2010, O’Gorman, P.A. et al. 2012), El Niño
91 and Southern Oscillation (ENSO) (L’Ecuyer et al. 2006), Madden-Julian Oscillation (MJO)
92 (Kim et al. 2015) to mesoscale convective system (MCSs) (Bouniol et al. 2016). This multiscale
93 coupling should be accurately represented for models to simulate atmospheric radiative heating
94 and cooling successfully. Failing to simulate the coupling of radiation-precipitation relationships
95 at each spatial and temporal scale yieldwill-bring large uncertainties in representing cloud cover,
96 precipitation (both stratiform precipitation and convective precipitation) and thermodynamic

97 | forcing-~~ete~~. (Wilcox et al. 2001; O'Brien et al. 2013; Betts et al. 2014; Calisto et al. 2014). The
98 | phase of ENSO and MJO coupling with large-scale global circulation may also be
99 | misrepresented and lead to large bias in climate models and reanalysis if the radiation-
100 | precipitation coupling relationship is not well represented (L'Ecuyer et al. 2006, Kim et al.
101 | 2015).

102 | The way that clouds and precipitation are currently parameterized and coupled in General
103 | ~~Global~~ Circulation Models (GCMs) is known to produce errors in radiative and latent heating
104 | distributions, ~~which are also two main parts of diabatic heating~~, such as insufficient low cloud
105 | cover in subtropical subsidence regions (Kay et al. 2012), warm sea surface temperature (SST)
106 | biases in the southeast Pacific (Yu and Mechoso 1999; Dai et al. 2003; Li et al. 2004), the
107 | presence of a ubiquitous tropical rain band south of the equator (Waliser et al. 2003; Masunaga
108 | and L'Ecuyer 2011), premature onset of deep convection particularly over land (Dai and
109 | Trenberth 2004; Grabowski et al. 2006; Clark et al. 2007), the lack of Madden-Julian Oscillation
110 | (MJO) (Lee et al. 2001), and underestimates of the Walker circulation response to El Nino
111 | (L'Ecuyer and Stephens, 2007; Kociuba and Power 2015). The role of the coupling cloud-
112 | radiation interaction also affects the simulation of the MJO (Kim et al. 2013) and can amplify the
113 | warm El Nino phases of the El Nino-Southern Oscillation (ENSO) (Radel et al. 2016).

114 | In addition to cloud-precipitation-radiation biases in climate models, reanalyses are also
115 | biased with respect to the observations~~there are also biases between reanalysis and observations,~~
116 | mainly due to the different assimilation methods and forecasting systems they use. even though
117 | reanalysis ~~is~~ are constrained by observations. ~~Reanalysis modeled~~ Clouds, radiation, and
118 | precipitation represented in reanalyses, ~~radiation, and precipitation~~ generally agree with
119 | observations at the global mean scale, however, large biases occur at the regional scale. Dolinar

120 et al. (2016) compared five reanalysis precipitation rates (PRs) with those from the Tropical
121 Rainfall Measurement Mission (TRMM) and found reanalysis PRs overestimate the large-scale
122 TRMM mean by 3% ~~-20~~ %, and also overestimate PRs in both ascent and subsidence regimes.
123 PR biases over the ascent regime are an order of magnitude larger than those over the descent
124 regime. Also, ~~the biases an uncertainty~~ in reanalysis caused by a lack of mid-level and/or low
125 clouds, ~~water vapor~~^{CWV}, anomalous temperature structures and overestimated atmospheric
126 stability represented by stronger subsidence result in both radiative and precipitation biases
127 (Naud et al. 2014; Griggs et al. 2008; Liu et al. 2016; Stengel et al. 2018). Both reanalysis and
128 some climate models may have cloud, convection, or boundary layer scheme problems that lead
129 to a large bias in individual weather systems and an inability to simulate the correct surface solar
130 radiation (Naud et al. 2014), as well as global precipitation (Bodas-Salcedo et al. 2007).
131 Approximations used in the model's representation of moist processes strongly affect the quality
132 and consistency of both cloud radiative ~~forcing-effect~~ (~~CRFCRE~~) and the hydrological cycle
133 (Dee et al. 2011; Bosilovich et al. 2017).

134 In some numerical models, such as the minimal model of a moist equatorial atmosphere
135 of Fuchs and Raymond (2001), the coupled ocean-atmosphere model of Bretherton and Sobel
136 (2002) and Sobel and Gildor (2003), they fixed the relationship between ~~CRFCRE~~ and
137 precipitation in radiative heating and cooling parameterization processes, assuming that clouds
138 reduce the clear-sky radiative cooling by an amount proportional to precipitation. This cloud-
139 radiation feedback parameter was determined by the Tropical Ocean Global Atmosphere
140 Coupled Ocean-Atmosphere Response Experiment (TOGA COARE) radiation dataset and fixed
141 at 0.2, but they note that the uncertainties are as large as 50%.

142 Emerging state-of-the-art satellite observations offer the opportunity to examine this
143 relationship in detail. In this context, L'Ecuyer et al. (2006) and Daloz et al. (2018) explored five
144 monthly mean cloud impact parameters (CIPs) based on both TRMM and A-Train satellite
145 observations that can connect the precipitation and cloud radiative effects to represent the cloud
146 processes in climate models better. There are two energy and water cycle coupling parameters in
147 the definition of CIPs, the surface cooling efficiency, R_c and atmospheric heating efficiency, R_h ,
148 representing how efficiently a precipitating cloud can cool the surface or heat the atmosphere,
149 respectively, per unit latent heat release from rainfall. These observational radiative efficiencies
150 were first used to show the evidence of cloud feedback pathways associated with ENSO in the
151 Pacific by L'Ecuyer et al. (2006). They demonstrated that clouds in the East Pacific heat the
152 atmosphere more efficiently and cool the surface less efficiently per unit rainfall with increasing
153 SST, suggesting that changes in cloud characteristics may reinforce changes in the Walker
154 circulation during El Niño events. Their estimates of R_c range from -0.7 to 0 and -0.1 to 0.4 for
155 R_h at the monthly scale, which is considerably different from the constant of 0.2 used in the
156 aforementioned modeling studies with biases greater than 100%. In Daloz et al. (2018), they
157 used A-Train observations and reanalyses to demonstrate the global distribution and climatology
158 of CIPs for ~~the first first the~~ time. The global mean spatial distributions of CIPs were compared
159 comprehensively, and while they briefly examined the relationship between CIPs and monthly
160 mean vertical pressure velocity at 500hpa (ω_{500}), there was little discussion on the relationship to
161 the thermodynamic environments or the variations in the strength off the coupling at different
162 time scales. As the cloud radiative feedback on atmospheric circulation is still one of the most
163 important topics in climate studies, the environmental impacts on CIPs should be studied in more
164 detail to help improve the performance of GCM and reanalysis (Bretherton et al. 2002,

165 Bretherton et al. 2005; Muller et al. 2012; Bony et al. 2015). Also, the high sensitivity of the
166 strength of the cloud-radiation feedbacks in the current models indicate that investigation of the
167 ratio between ~~CRFCRE~~ and precipitation in observation can provide a reference for model
168 designers (Ying et al. 2016).

169 One of the key obstacles to accurately understanding the feedback processes of clouds in
170 climate is their dependence on the environments in which the clouds reside (Stephens 2005).
171 Studies show that different cloud regimes, which determine the sign and strength of coupled
172 CIPs (discussed more later), are associated with both dynamical and thermodynamical
173 environmental variables, such as SST (Xu et al. 2009, Eitzen et al. 2010), ~~column water vapor~~
174 ~~(CWV)~~ and ω_{500} . Correspondingly, they also influence the coupling between precipitation and
175 radiation (Wang ~~and Sobel et al.~~ 2011). Kubar et al. (2012) reported a strong correlation between
176 low topped cloud fractions and SST and ω_{500} . They also found that the correlation increased with
177 increasing averaging time scales (Kubar et al 2012). Their findings indicate that when
178 environmental variables change, such as SST and ω anomalies during an ENSO event, the
179 fraction of clouds should change, leading to a corresponding change of cloud radiative forcing,
180 which may strengthen or dampen large-scale circulation and impact precipitation intensity. This
181 suggests further study of the coupling ~~CRFCRE~~ and precipitation with the environment is
182 needed. In addition, the coupling of ~~CRFCRE~~ and precipitation is needed in environmental
183 control experiments (Larson et al. 1999) because both ~~CRFCRE~~ and precipitation are susceptible
184 to changes in SST and water vapor (Larson et al. 1999, 2003a, 2003b). However, in modeling
185 experiments, they are often tested separately instead of coupled. Additionally, radiative
186 heating/cooling and precipitation are constrained under radiative-convective equilibrium (RCE).
187 Studies show that under RCE assumption, temperature and water vapor have positive feedback in

188 atmospheric longwave cooling (Allan 2009; Allan 2011; Pendergrass and Hartmann 2014;
189 Colman, 2015), but L'Ecuyer et al. (2006) demonstrated that RCE cannot be met locally due to
190 the highly variable nature of frequency, structure, and radiative properties of clouds and
191 precipitation, which also motivates further examination of the dependence of coupled CIPs on
192 the environment. ~~Furthermore, studies on the observations of the coupling in CRF and~~
193 ~~precipitation and their environment can be a good complement to sub-grid clouds parameter~~
194 ~~represented in climate models.~~

195 Overall, the main goal of this study is to evaluate the range of energy and water cycle
196 coupling CIPs in both A-Train satellite and reanalysis datasets and to understand how they are
197 linked to the dynamic and thermodynamic environment. A comparison in the global distribution
198 of A-Train-derived and reanalysis-derived coupling CIPs at different time scales is ~~is~~ first
199 conducted. Given the aforementioned important links between the environment and
200 precipitation, radiation and their coupling, the analysis of Daloz et al. (2018) is expanded to also
201 include not only the CIP relationship with ω_{500} , but also SST and CWV. Observational and
202 reanalysis coupling CIPs are conditionally sampled by matched environmental variables to
203 determine how well reanalyses capture interactions among radiation-precipitation coupling,
204 thermodynamic environments, and the corresponding large circulation. Profiles of humidity, air
205 temperature and vertical velocity profiles are then analyzed to reveal how reanalysis differences
206 in environmental states are linked to coupled CIP differences from the observations. Then the
207 ~~observational and reanalysis coupling CIPs are conditionally sampled by environmental variables~~
208 ~~SST, CWV and ω_{500} to determine how well reanalyses capture interactions among radiation-~~
209 ~~precipitation coupling, thermodynamic environments, and the corresponding large circulation~~
210 ~~indicated by ω_{500} .~~

211

212 **2. Data and Methodology**

213 **2.1 Satellite observations**

214 The coupled CIPs are calculated from standard CloudSat-CALIPSO data products,
215 including 2B-FLXHR-LIDAR (Stephens et al. 2002 and 2008; L'Ecuyer et al. 2008), 2B-
216 GEOPROF-LIDAR (Stephens et al. 2002, 2008 and 2017; Sassen et al. 2008; Mace et al. 2009)
217 and 2C-RAIN-PROFILE (Lebsock and L'Ecuyer 2011), and the Advanced Microwave Scanning
218 Radiometer–Earth Observing System (AMSR-E) rainfall product, AE_RAIN (Wilheit 2003;
219 Kummerow et al. 2010). CloudSat is a polar-orbiting satellite with a 98° orbital inclination
220 carrying a 94 GHz (W-band) Cloud Profiling Radar (CPR), which is used to probe the vertical
221 structure of clouds and precipitation (Stephens et al. 2008; Stephens et al. 2017; L'Ecuyer and
222 Jiang 2010; Mace et al. 2014). CALIPSO uses the cloud-aerosol lidar with orthogonal
223 polarization (CALIOP) to probe the vertical structure and properties of thin clouds and aerosols.
224 With the combination of both CPR and CALIOP, there is an improved ability to detect thin
225 cirrus and low clouds, especially when multiple layered clouds exist. The 2B-GEOPROF-
226 LIDAR dataset provides the cloud layer and cloud top information to distinguish the heights and
227 the number of cloud layers. The precipitation is provided by the 2C-RAIN-PROFILE dataset,
228 which uses the two-way path integrated attenuation (PIA) of the entire atmospheric column to
229 determine the presence of precipitation within the column (Haynes et al. 2007; Haynes et al.
230 2009; Stephens et al. 2008; Lebsock et al. 2011). However, the CPR has limitations in detecting
231 heavy rain because of attenuation (Behrangi et al, 2012). To mitigate this limitation, rain rate
232 derived from AMSR-E observations is used whenever the AMSR-E rain rate exceeds 2C-RAIN-
233 PROFILE. AMSR-E is a total power passive-microwave (MW) radiometer system on board

234 NASA EOS Aqua satellite with twelve channels and six frequencies measuring brightness
235 temperature at 6.925, 10.65, 18.7, 23.8, 36.5 and 89.0GHz. Rain rate and rain type over ocean
236 are from the AE_RAIN products generated via the Goddard Space Flight Center (GSFC)
237 Profiling algorithm (GPROF2010) (Wilheit 2003; Kummerow et al. 2010; Kummerow et al.
238 2015). This study uses an existing rainfall subset that collocated AMSR-E rainfall products with
239 the CloudSat track (Global Hydrology Resource Center/MSFC/NASA, 2009). One thing to note
240 is that currently the CloudSat 2C-RAIN-PROFILE dataset is only applied over ocean (Lebsock
241 et al 2011), so the coupled CIPs are only calculated over the ocean.

242 Radiative fluxes are used in the calculation of coupled CIPs and are provided by 2B-
243 FLXHR-LIDAR (Stephens et al. 2008; L'Ecuyer et al. 2011), referred to hereafter as 2BFLX.
244 2BFLX blends information from the A-Train constellation including CloudSat's CPR, the
245 CALIPSO satellite's CALIOP, and the Moderate Resolution Imaging Spectroradiometer
246 (MODIS) and AMSR-E instruments on the Aqua satellite to generate vertically-resolved profiles
247 of broadband radiation using a radiative transfer model (L'Ecuyer et al. 2008; Henderson et al.
248 2013). The 2BFLX algorithm, with the combination of multisensor observations, brings a more
249 accurate and comprehensive perspective in determining the radiative impacts of clouds and
250 aerosols.

251

252 **2.2 Reanalyses**

253 This study compares the coupled CIPs from two modern reanalyses, MERRA-2 and
254 ERA-Interim with A-Train derived products from September 2006 – December 2010 for 60°S -
255 60°N. The relationship between the environment and coupled CIPs is also evaluated.

256

257 2.2.1 *MERRA-2*

258 MERRA-2 (Gelaro et al. 2017; Bosilovich et al. 2015b; Bosilovich et al. 2016;
259 Bosilovich et al. 2017) replaces the previous MERRA with increased resolution, improvements
260 in the GEOS-5 model, and in the assimilation system. The new system enables assimilation of
261 modern hyperspectral radiance and microwave observations as well as GPS-Radio Occultation
262 datasets, and is the first long-term reanalysis that assimilates space-based observations of
263 aerosol. After 2005, ozone observations are included. Several upgrades have been made to the
264 physical parameterization schemes including an increase in reevaporation of frozen precipitation
265 and cloud condensate (Molod et al. 2015). The new reanalysis dataset now contains a Tokioka-
266 type trigger ([Bacmeister and Stephens, 2011](#)) on deep convection as part of the relaxed Arakawa-
267 Schubert convective parameterization (Moorthi and Suárez 1992; Cullather et al. 2014). In our
268 studies, we use `tavg1_2d_rad_Nx` 1-hourly time-averaged data to calculate the radiative fluxes at
269 surface and atmosphere and total precipitation from `tav1_2d_flx_Nx` 1-hourly time-averaged
270 data to calculate the latent heating.

271

272 2.2.2 *ERA-Interim*

273 ERA-Interim (Dee et al. 2011) is a global atmospheric reanalysis beginning in 1979,
274 developed by the European Center for Medium Range Forecasts (ECMWF). ERA-Interim
275 replaced the previous reanalysis dataset from the ECMWF, ERA-40. Between ERA-40 and
276 ERA-Interim, changes to the convective and boundary layer cloud schemes were made. For
277 example, the convective cloud scheme can now be triggered at night, which increases its
278 atmospheric stability and therefore creates less precipitation (Dee et al. 2011). The new moist
279 boundary layer scheme reduces the underestimate of stratocumulus clouds because of changes in

280 the inversion strength and height (Kohler et al. 2011). Convection, vertical motion, radiative
 281 heating and turbulence are connected to cloud generation via the prognostic cloud scheme (Jakob
 282 1998). The Rapid Radiative Transfer Model computes radiation (Mlawer et al. 1997). In this
 283 study, we use the 3-hour surface flux variable and surface albedo to get the downward shortwave
 284 flux and the reflected upward shortwave flux. Radiative flux variables at- the top of atmosphere
 285 (TOA) are obtained directly from ERA-Interim. Total precipitation from ERA-Interim is used to
 286 calculate the latent heating. ERA-Interim also provides the environmental variables, SST, CWV,
 287 ω_{500} , which are used as the environmental variables that are matched with coupled CIPs.

289 2.3 Calculations of Coupled CIPs

290 Two coupled CIPs are calculated with the shortwave and longwave CRFCRE from
 291 2BFLX and the coincident CloudSat/AMSR-E precipitation. The radiative cooling efficiency, R_c ,
 292 at the surface (SFC) is defined as:

$$293 \quad R_c = \frac{F_{SW,SFC,all}^{\downarrow} - F_{SW,SFC,clear}^{\downarrow}}{LH} \quad (1)$$

294 where $F_{SW,SFC}^{\downarrow}$ is the downwelling shortwave (SW) flux that is evaluated in both clear-sky and all-
 295 sky conditions. Subscripts ‘clear’ and ‘all’ correspond to clear-sky and all-sky conditions
 296 respectively. R_c represents a cloud’s ability to cool the surface per unit LH from rainfall, where
 297 LH is defined as the column latent heating from the precipitation reaching the surface and is
 298 calculated as

$$299 \quad LH = \rho * Lq_v * RR \quad (2)$$

300 where ρ is the density of water, Lq_v is latent heat of vaporization for water, and RR is the
 301 average surface rainfall rate from CloudSat or AMSR-E. Similarly, the atmospheric radiative
 302 heating efficiency R_h describes a cloud’s ability to heat the atmosphere per unit LH,

Formatted: Font: 12 pt

Formatted: Font: 12 pt

Formatted: Font: 12 pt

Formatted: Font: 12 pt

Formatted: Font: 12 pt

Formatted: Font: 12 pt

Formatted: Font: 12 pt

Formatted: Font: 12 pt

Formatted: Font: 12 pt

$$R_h = \frac{(\Delta F_{LW} - \Delta F_{SW})_{all} - (\Delta F_{LW} - \Delta F_{SW})_{clear}}{LH} \quad (3)$$

303 where $\Delta F_{LW} = F_{LW,SFC}^\uparrow - F_{LW,SFC}^\downarrow - F_{LW,TOA}^\uparrow$ and

304 $\Delta F_{SW} = F_{SW,TOA}^\downarrow - F_{SW,SFC}^\uparrow - F_{SW,SFC}^\downarrow - F_{SW,TOA}^\uparrow$ are the longwave(LW) and SW atmospheric
 305 radiative flux divergences, respectively, calculated between the SFC and top-of-atmosphere
 306 (TOA). Clearly, you can see that the numerator of R_c is the cloud forcing at surface, that is, the
 307 amount of incoming solar radiation that has been hindered by the clouds. The numerator of R_h is
 308 the total CRECRE of the atmosphere, while the denominator of both equations is latent heating
 309 that has been released by the precipitation from the clouds.

310 We use 2BFLX to calculate the numerators of Equation (1) and Equation (3) during the
 311 daytime. The combination of 2C-RAIN-PROFILE and AMSR-E data provide surface
 312 precipitation rate from which we can estimate latent heating as in Equation (2). Again, due to the
 313 known limitations of the 2C-RAIN-PROFILE dataset in heavy rain scenarios, AMSR-E-
 314 CloudSat collocated products are used when the CPR is judged as saturated based on a flag in the
 315 algorithm. Otherwise, the CPR rain rate is used because CloudSat has a superior ability in
 316 detecting light and moderate rain (Behrangi et al. 2012; Lebsock et al. 2011).

317 Because the reanalysis precipitation is calculated based on the moisture budget and must
 318 meet the budget equilibrium, sometimes the precipitation has a rather small value in one grid
 319 box. As Stephens et al. (2010) discussed, models produce precipitation approximately twice as
 320 often as that observed and make too much light rainfall. The reanalysis products analyzed here
 321 provided values as small as 10^{-12} mm/hr, which is well below any space borne precipitation
 322 sensor detection limits and also produces unrealistically large values of R_c and R_h . Here we use
 323 the minimum precipitation value of 0.01 mm/hr for each grid box, which is the statistical
 324 minimum value of precipitation after sampling the CloudSat/AMSR-E precipitation for a grid

Formatted: Indent: First line: 0.5"

325 box. This threshold is used to filter precipitation in reanalysis; however, we tested different
326 thresholds and while there are expected changes in the quantitative value, the overall patterns
327 and conclusions of this study are not dependent on the choice of threshold. To compare the
328 different reanalysis datasets to each other and to the observations, we download ERA-Interim
329 and MERRA-2 dataset at $2.5^\circ \times 2.5^\circ$ directly with inherent interpolation. Meanwhile, all the A-
330 Train data are also averaged to a common $2.5^\circ \times 2.5^\circ$ grid at 3-hourly temporal resolution. Each
331 pixel from A-Train datasets is matched to the nearest 3-hourly time step of the reanalysis
332 datasets.

333

334 **3. Global coupled CIPs distributions**

335 An overview of the global distribution of coupled CIPs from A-Train, ERA-Interim and
336 MERRA-2 is presented in Figure 1. These differ from the global patterns presented in Daloz et
337 al. (2018) in a significant way. Daloz et al. (2018) used monthly-averaged radiation and
338 precipitation to derive R_c and R_h . While these values are useful for identifying climatological
339 biases that result from systematic differences in cloud and precipitation PDFs, at these long
340 timescales radiation and precipitation may not be directly coupled. For example, it would be
341 possible to capture the same monthly mean value of the coupled CIPs with compensating errors
342 in the distribution of clouds and the wrong clouds producing precipitation. To more directly
343 explore the connection between precipitation and radiation on the timescales of the clouds and
344 the timescales for which the parameterizations must operate in the reanalyses, patterns of three
345 hourly-averaged results are shown in Figure 1. They are similar to the patterns calculated from
346 monthly mean fluxes, but differ in magnitude, since precipitation varies more temporally and
347 spatially than the radiative flux. As a result, when R_c and R_h are calculated at shorter time scales,

348 the variation of R_c and R_h is larger than that of the monthly average timescale shown in Daloz et
349 al. (2018).

350 From A-Train observations, there are clear patterns that correspond to the global
351 distribution of predominant cloud regimes. Generally, marine stratocumulus regions in the south
352 and north Pacific and south or west Atlantic (Wood et al. 2012; Hartmann et al. 1993), where
353 clouds cool the surface and atmosphere most efficiently because precipitation is weak,
354 correspond to the strongest negative R_c and R_h . ~~Over the ITCZ and South Asia monsoon region,~~
355 ~~R_h is large and R_c is small.~~ The Indo-Pacific warm pool region (white rectangle in Fig. 1) shows
356 strong R_c and R_h , which means that deep convection cools the surface and heats the atmosphere
357 more efficiently per unit rainfall. In shallow cumulus regions (180°W~135°W, 10°S~25°S), both
358 R_c and R_h are weaker than other regions. Note that polar regions (beyond 60°N or 60°S), are
359 removed due to the lack of liquid surface precipitation (Stephen et al. 2008; L'Ecuyer et al. 2010;
360 Lebsock and L'Ecuyer 2011; Mace et al. 2009; Mace et al. 2014) that results in too few samples
361 in each grid box to provide meaningful results.

362 Comparison with ERA-Interim and MERRA-2 in Figure 1 shows the global patterns are
363 generally consistent, although some tropical regions show significant differences between A-
364 Train and the reanalyses. One of these main biases appears over the Indo-Pacific warm pool.
365 Reanalyses generally fail to simulate both large R_c and R_h there, ~~although the reanalyses does~~
366 ~~generally capture strong R_h over the South Asia (India) monsoon region, although not as strong~~
367 ~~as the A-Train estimates.~~ One possible reason, at least for ERA-Interim, is that it underestimates
368 the LW CREFCRE at TOA over tropical regions due to biases in cloud fraction and the TOA
369 radiative flux diurnal cycles. Moreover, ERA-Interim overestimates precipitation in both
370 ascending and descending regimes (Itterly et al 2014; Dolinar et al 2016). Fig 1c indicates that

371 ERA-Interim R_c is generally stronger than other products over marine stratocumulus regions,
372 which is likely caused by the SW biases reported by Dolinar et al. (2016). Meanwhile, Fig 1f
373 illustrates that CloudSat and ERA-Interim R_h is generally more negative than MERRA-2 over
374 marine stratocumulus regions, which is likely caused by underestimating the cloudiness over
375 marine stratocumulus areas in MERRA-2 reported by Hinkelman (2019). Also, it has been
376 reported that there is stronger water cycle in MERRA-2 than the observations because
377 modifications in the MERRA-2 model resulted in changes in ocean evaporation and atmospheric
378 transport and excessive precipitation is generated in the Indo-Pacific warm pool (Bosilovich et
379 al. 2015; Bosilovich et al. 2017; Gelaro et al. 2017). This may also explain why MERRA-2 R_h is
380 slightly smaller than ERA-Interim over ~~the Indo-Pacific warm pool~~~~the South Asia (India)~~
381 ~~Monsoon region~~. Other differences appear over eastern Pacific marine stratocumulus region,
382 where reanalyses generally produce stronger R_c over a larger region, which means that the clouds
383 cool the surface more efficiently per unit rainfall. While reanalyses are constrained by
384 observations, such biases may have significant implications for freely running GCMs since the
385 regional variations in R_c and R_h feedback on the large-scale circulation ~~and could increase the~~
386 ~~potential lack of response to El Niño events~~. It also implies some limitations of models to
387 represent the Walker and Hadley Circulations (L'Ecuyer et al. 2006).

388 As previously mentioned, due to the sampling limitations of the sun synchronous A-Train
389 satellites, R_c and R_h values were only compared with reanalysis for grid boxes with satellites
390 overpasses. While not shown here, R_c and R_h can be calculated from the full diurnal cycle
391 available in the reanalyses. The climatological global patterns of the reanalyses are ~~still~~ similar
392 and still highly depend on the distributions of the cloud regimes, however the regional

393 differences with observations are amplified with even weaker R_h and R_c in the warm pool and
394 stronger R_h and R_c in subsidence regimes and the southern oceans.

395 ~~Figure 2 summarizes the zonal mean of both R_c and R_h . R_c in both reanalyses is generally
396 more consistent than R_h , but there are obvious differences between A-Train and the reanalyses.
397 For R_c , A-Train has a larger value in the mid-latitude from 30° N and 60° N. The difference is
398 caused by the underestimate of R_c over warm pool region by reanalyses discussed in Figure 1,
399 but may also be related to precipitation biases. Over tropical areas, the bias between A-Train
400 observations and reanalysis, as we have discussed, can also be clearly shown. The peak value of
401 R_h in ERA-Interim, comparing with A-Train and MERRA-2, is more equatorial which could
402 result from a relatively narrower Hadley Circulation simulated by ERA-Interim than with other
403 reanalysis datasets (Nguyen et al. 2012).~~

404 Figure 2 demonstrates the time-scale dependence of R_c and R_h across daily to long-term
405 (here 3 months) averaging time scales for the three different cloud regimes, deep convection,
406 shallow cumulus, and stratocumulus, outlined in Figure 1. In each region, the absolute magnitude
407 of both R_c and R_h decrease with increasing averaging time scales. At monthly or longer
408 timescales, coupled CIP value are small and differences between the reanalyses and observations
409 are also relatively small. However, as the averaging time scales decrease, the model-
410 observational differences increase in most cloud regimes, but especially in the warm pool region.
411 The top panels show that the precipitation-radiation coupling in deep convective regions, in
412 particular, is not well-captured at the shorter time scales of the convection and both reanalyses
413 have significantly weaker CIP than observed. The biases in greenhouse effect, surface SW CRE,
414 and precipitation each also increase with averaging timescale (not shown), however, not to the
415 degree of R_c and R_h . This suggests that these increasing biases with shorter averaging timescales

Formatted: Indent: First line: 0"

416 are not due just radiation or precipitation, but rather their coupling in the reanalyses. Differences
417 in the low cloud regimes are smaller, with the shallow cumulus regime showing similar but
418 weaker patterns to deep convection. In stratocumulus regions, the biases are more constant with
419 averaging timescale, likely representing the relatively persistent (in both space and time) cloud
420 decks with little precipitation.

422 4. **4. Environmental regime dependence**

423 The previous figures indicate differences in the coupling between radiation and
424 precipitation is associated with cloud regime. Because both cloud regimes (Bony et al. 2004) and
425 precipitation, and correspondingly, the strength of latent heating have a strong relationship to the
426 environment (Huaman and Schumacher 2017), to understand the drivers in the spatial patterns
427 we analyze the relationship between coupled CIPs and several proxies often used to characterize
428 synoptic environment, including both thermodynamic variables (SST and CWV) and dynamic
429 variable (vertical pressure velocity at 500hpa (ω_{500}), which is a proxy for the large-scale
430 overturning circulation).

431 The relationships between R_c and R_h and these environmental variables are shown in
432 Figure 33. In the left panels, A-Train results show that R_c is relatively strong at low SSTs and
433 then weakens (represented by an increase) with increasing SST until about 295-300 K. After
434 this, R_c rapidly decreases with increasing SST representing a strong cooling efficiency
435 enhancement. In the results of both reanalyses, the trends at moderate and high SSTs are
436 completely opposite. At low SSTs they both show strengthening R_c , however R_c continues to
437 become strong until SSTs reach around 295 K, at which point they rapidly weaken. One of the
438 reasons for the lack of strong R_c in the reanalyses at high SSTs is that, as previously discussed,
439 over the Indo-Pacific warm pool region, where SST is typically over 300 K, both reanalyses fail

Formatted: Normal, No bullets or numbering

Formatted: Font: Bold

440 to simulate the strong R_c that is shown by A-Train. This suggests that the reanalyses do not
441 accurately couple the storm-scale precipitation and cloud radiative effects at high SSTs, either
442 producing too much precipitation or too weak shortwave cloud radiative forcing. Another
443 difference is in the position of the first minimum, which occur at similar SST for both reanalyses
444 but occurs at a much lower SST for A-Train. This discrepancy results from the differences in the
445 extent of the regions demonstrating relatively large R_c in A-Train and reanalysis. The position of
446 the first minimum is determined by strong R_c over the marine stratocumulus region and mid-
447 latitudes. Strong R_c over marine stratocumulus regions is confined to the Southern Ocean and
448 regions along the coast where SSTs remain relatively low in the A-Train results. In the rest of
449 subtropics and in the southern hemisphere extratropics, A-Train reports a lower R_c . The global
450 distributions in Figure 1 show that regions of large R_c in reanalyses expand farther from the
451 coasts toward the center of the ocean basins where SSTs are much warmer. However, reanalyses
452 tend to produce lower cloud albedo and more precipitation over warmer SST regions. The
453 differences combine make the R_c lower into regions of warmer SSTs. By contrast, the patterns of
454 R_h associated with SSTs in the three datasets don't vary as much with R_h increasing with
455 increasing SSTs. Reanalyses exhibit a relatively lower range although they switch from low
456 clouds that cool the atmosphere to clouds that heat the atmosphere at different SSTs with A-
457 Train falling in between the two reanalyses. In general, the reanalyses show more atmospheric
458 cooling per unit rainfall at low SSTs associated with shallow, warm rain system and less
459 atmospheric heating at high SSTs, likely associated with deficiencies representing deeper and
460 high cloud anvils or overestimating convective precipitation. The large differences between A-
461 Train and the reanalyses simulating R_h at high SSTs is consistent with the differences shown

462 over the warm pool area in Figure 1 and suggests that the reanalyses underestimate the strength
463 of the coupling in deep convective cloud systems typical of this region.

464 In Figure 3e3c-d, the relationship between CWV and the coupled CIPs for the three
465 datasets is shown. The patterns are similar to SST in all the three datasets, where R_c of A-Train
466 has two minima but both reanalysis results only have one. It is not surprising that the results
467 indicate the change in coupled CIPs with CWV is very similar to SST since the correlation
468 coefficient between SST and CWV is 0.81 in ERA-Interim and 0.79 in MERRA2, respectively in
469 the matched dataset. However, from these plots, it is unknown which is the main driver. Many
470 studies (Zhang et al. 1996; Bony et al. 2015; Trenberth et al. 2010) have shown a strong
471 relationship between cloud radiative effects and SST, but studies also show a strong relationship
472 between CWV and precipitation/latent heating (Bretherton et al. 2004; Peters and Neelin 2006;
473 Neelin et al. 2009; Holloway and Neelin 2009; Ahmed and Schumacher 2015, 2016). However,
474 from previous studies (Bony et al. 2004; Jakob et al. 2003; Jakob et al. 2005; Stephens 2005;
475 Voigt and Shaw 2015), we know that both SST and CWV can contribute to the ~~CRE~~CRE and
476 precipitation via different mechanisms, so a joint distribution of R_c and R_h with both variables is
477 examined later in Figure 4-6 to determine which one is dominant in controlling R_c and R_h .

478 The link between coupled CIPs and dynamical regime is shown in Fig 3e3e-f. Figure 3e
479 3e shows that R_c decreases as ω_{500} increases from negative (ascending regimes) to positive
480 (subsidence regimes). Convective cloud regimes are generally associated with strong upward
481 motion and typically accompanied by large precipitation and latent heat release, corresponding to
482 a smaller R_c (assuming that the cloud forcing on the surface does not change). Positive ω_{500} is
483 generally associated with a more stable atmosphere and the formation of low stratiform clouds
484 where precipitation is usually small, but the cloud forcing on the surface could be very large

485 leading to increased R_c . Both the observations and the reanalyses behave similarly, although they
486 are closer in moderate ascending regimes than in subsidence regimes where A-Train results
487 becomes much weaker than the two reanalysis estimates. Figure 3f shows that upward motion
488 and downward motion obviously control the sign of R_h , and strong ascent regimes where A-Train
489 estimate is a little bit stronger. From the results of R_h , upward motion and downward motion
490 obviously control the sign of R_h . For ascent regimes, R_h is positive and cloud heat the atmosphere
491 more efficiently due to the enhancement of cloud greenhouse effect associated with deep
492 convective clouds. For subsidence regimes, R_h is negative because the boundary layer tends to be
493 more stable in these regimes and supports the formation of stratocumulus clouds, which will cool
494 the atmosphere efficiently and produce little precipitation. Like R_c , the range of R_h estimates
495 from A-Train and reanalyses appear to be closer in moderate ascent regimes than in the
496 subsidence regimes and strong ascent regimes.

497 Given the large differences between observations and reanalyses in the tails of the curves
498 in Figure 3, the relative frequency of occurrence in each environmental bin is shown in Figure 4.
499 The ERA-Interim and MERRA2 distributions are quite similar suggesting the reanalyses produce
500 atmospheric states with similar frequencies, although that is not necessarily indicative of how
501 these states are coupled with precipitating convection and will be examined more later. There
502 are clearly fewer samples in the tails of these distributions with few SST values above 302K or
503 below 280K, few CWV values above 60 kg m⁻² or below 10kg m⁻², and few ω_{500} values above
504 0.3 Pa/s and below -0.5 Pa/s. However, during data processing, we required a minimum of at
505 least 100 samples for analysis and many of these bins still have hundreds to thousands of
506 samples. While these environmental states are relatively rare and tend to be associated with very

507 | strong ascent or descent, they should not be neglected since they are often accompanied by some
508 | of the most extreme weather.

509 |
510 | Given the strong covariability in SST, CWV, and dynamic regimes, it is not surprising
511 | that R_c and R_h appear to be influenced by more than one environment variable. In an attempt to
512 | determine which is the controlling variable, Figures [4-5](#) and [5-6](#) show the joint distributions of
513 | mean coupled CIPs conditionally sampled by combinations of different environmental variables.
514 | The first two rows of Fig. [4-5](#) show that the strength of R_c is largely controlled by the dynamic
515 | environment and that the observations and reanalyses are generally consistent. Clouds have
516 | strong cooling efficiencies in subsidence regimes and weak ones in ascent regimes. Within the
517 | ascent regime the observations show enhanced cooling with thermodynamic regime changes,
518 | while the reanalysis shows a steady weakening which appears to be more controlled by CWV
519 | than SST especially in MERRA-2. In the subsidence regimes, A-Train shows a steady
520 | weakening of R_c beginning at moderate SST and CWV, which is not shown in the reanalyses.
521 | This is likely due to the expansion of the regions of large R_c away from the coast and toward
522 | regions of greater SST and CWV shown by the reanalyses in Figure 1. The relationship between
523 | R_c and the thermodynamic environment echoes the considerable differences between A-Train
524 | observations and reanalyses shown in Figure [33](#). The reanalyses appear to be somewhat more
525 | horizontally stratified, which indicates that CWV is a stronger control on R_c than SST in the
526 | reanalyses compared to the observations. In the observations, below about 290K it is difficult to
527 | discern which thermodynamic variable is controlling R_c . For SST above 290K, holding SST
528 | fixed shows increasing R_c with CWV in observations and decreasing in reanalyses. Holding
529 | CWV fixed with increasing SST shows little variation in reanalyses, suggesting that ~~above 290K~~

530 CWV appears to control the strength of R_c . These results also indicate that the observations show
531 much more distinction between the controls on cooling efficiencies in different cloud regimes,
532 while the reanalyses vary much more smoothly from one regime to another.

533 R_h in Figure 5-6 shows that clouds have strong positive heating efficiencies in ascent
534 regions ~~like the Indo-Pacific warm pool region~~ and strong negative heating efficiencies in
535 subsidence regimes, ~~such as those dominated marine stratocumulus~~. The sign of R_h is largely
536 controlled by the dynamic environment, which is also consistently shown in both A-Train
537 observations and reanalyses. ~~Clouds have strong negative heating efficiencies in subsidence
538 regimes and strong positive heating efficiencies in ascent regimes~~. Within the ascent regime, A-
539 Train results show an obvious trend in enhanced heating associated with the thermodynamic
540 regime changes while the reanalysis show only a moderate enhanced heating, which is weakest
541 in MERRA-2. This is likely due to the failure of reanalyses to simulate high R_h over warm pool
542 regions as in Figure 1. From the last row of this figure, the observations demonstrate that clouds
543 become increasingly efficient at heating the atmosphere per unit rain, especially in deep
544 convective cloud regimes, in regions of ascent with high SST and CWV. The observations are
545 also much more vertically stratified, indicating that CWV is a stronger control than SST in the
546 observations compared to the reanalyses. we can see that both the results of R_c and R_h indicate
547 that CWV is a stronger control on both R_c and R_h than SST in the reanalyses compared to the
548 observations. For R_h , even when SST increases beyond 300K, if there is not sufficient CWV, R_h
549 shows little strengthening. But when CWV is sufficient, the strength of R_h rapidly increases. It
550 demonstrates that clouds will heat the atmosphere more efficiently per unit rain, especially in
551 deep convective cloud regimes, with both high SST and CWV. Also, when CWV increases,
552 longwave emission to the surface decreases and the cloud greenhouse effect increases with the

Formatted: Indent: First line: 0.5"

553 ~~increase of cloud thickness and cloud top. The strength of the large scale circulation has a strong~~
554 ~~control on the magnitude of R_e , but with the strongest cooling at the tails of the SST/CWV~~
555 ~~domains. The sign of R_h is controlled by the large scale circulation, while CWV appears to~~
556 ~~dominate in controlling the strength of R_h rather than SST.~~

557 While Figure 5 shows that the reanalyses produce generally similar distributions of
558 environments, Figure 3.5, and 6 suggest there are either differences in the environments in which
559 the precipitating clouds occur or differences in the coupling between precipitation and radiation
560 associated with a given atmospheric state in the reanalyses. Figure 7 shows the zonal mean
561 difference (ERA-Interim minus MERRA-2) of air temperature, specific humidity, and ω profiles
562 from the samples matched to A-Train precipitating clouds. While there are some hemispheric
563 differences, the main patterns show that in the tropics and subtropics, ERA-Interim has a warmer
564 temperature in the lower troposphere and lower temperature in the upper troposphere, suggesting
565 a more stable atmosphere in MERRA-2. This is consistent with the negative omega differences
566 across the tropics in Figure 7c, which means MERRA-2 has weaker ascent than ERA-Interim. In
567 the subtropics where ω is typically positive, these negative differences mean MERRA-2 has
568 stronger subsidence than ERA-Interim. The hemispheric differences in specific humidity are
569 larger, but with the exception of the lower troposphere in the northern midlatitudes, the
570 atmosphere is generally moister in MERRA-2. Along with the previous figures, this figure
571 suggests that differences in the atmosphere in which convection occurs as well as how the
572 precipitation-radiation coupling manifests in the various atmospheric states both contribute to the
573 differences with observations. However, the environmental differences are relatively small and
574 the differences between the observations (which have been matched to the reanalysis states) and

575 reanalyses heating and cooling efficiencies in the previous figures suggests that the latter may be
576 more important.

577 **5 Summary and discussions**

578 In this paper, we use A-Train observations and reanalyses to study two coupled CIPs, R_c
579 and R_h , that connect the surface and atmospheric CREFCRE and precipitation. Not surprisingly, R_c
580 and R_h vary with different cloud regimes. In regions dominated by stratocumulus clouds, they
581 tend to cool the surface and atmosphere more efficiently per unit latent heating release because
582 stratocumulus regions have low rain rates and highly reflective clouds that results in large cloud
583 SW radiative forcing. In this situation, both strong SW CREFCRE and low rain rate contribute to
584 strengthen R_c . For regions associated with deep convective clouds in environments with strong
585 ascent and sufficient CWV, observations show that clouds cool the surface and heat the
586 atmosphere more efficiently per unit latent heat release than the regions where there is weak
587 ascent or low CWV. Elevated and highly reflective cloud tops and large cirrus anvils enhance
588 both the cloud greenhouse effect and the cloud SW radiative cooling at surface.

589 Comparison between A-Train observations and coupled CIPs in ERA-Interim and
590 MERRA-2 show that they generally have similar global patterns. However, as model
591 parameterizations are challenged with simulating different cloud regimes, we found some
592 possible limitations of reanalysis data in coupling cloud radiative effects and precipitation over
593 deep convective cloud regions. Both ERA-Interim and MERRA-2 show weaker R_c and R_h over
594 the warm pool area where deep convective clouds prevail. The lower R_h values result from an
595 underestimate of the LW CRE at TOA over tropical regions and overestimate of precipitation.
596 Moreover, when the coupled CIPs are composited for increasingly shorter time scales, there are
597 larger biases in reanalysis coupled CIPs compared with observation than was shown for

598 calculations at longer timescales (Daloz et al. 2018), so we suspect that the reanalyses are
599 challenged more in capturing the coupling between the radiation and precipitation for convective
600 systems with shorter timescale variability, such as convectively-coupled waves.

601 Observation data inevitably have some uncertainties due to assumptions in the retrieval
602 algorithms. For instance, 2BFLX partly overcomes the uncertainties in the radiative effects
603 caused by low clouds, cirrus and aerosols, but some uncertainties remain in the SW and LW
604 fluxes. The former is primarily the result of uncertainties in LWC estimates, and the latter is
605 linked to errors in prescribed skin temperature and the lower-tropospheric water vapor
606 (Henderson et al. 2013). These uncertainties should be considered when comparing observational
607 results and reanalysis or model outputs; however, Henderson et al. (2013) showed relatively
608 good agreement between CERES and 2BFLX although it should be noted that differences
609 become relatively larger at shorter temporal and smaller spatial averaging scales. Estimates from
610 different observation systems in the future could help reduce these observational
611 uncertainties.~~We also evaluated coupled CIPs in ERA-Interim and MERRA-2 and find that they~~
612 ~~generally have similar global patterns as the observations. As models are always faced with the~~
613 ~~challenge of simulating different cloud regimes, we found some possible limitations of reanalysis~~
614 ~~data in coupling cloud radiative effects and precipitation over deep convective cloud regions.~~
615 ~~Both ERA-Interim and MERRA-2 show weaker R_e and R_r over the warm pool area where deep~~
616 ~~convective clouds prevail. The lower R_r values result from an underestimate of the LW CRF at~~
617 ~~TOA over tropical regions and overestimate of precipitation. Moreover, when the coupled CIPs~~
618 ~~are composited for shorter time scales, there are larger biases in reanalysis coupled CIPs~~
619 ~~compared with observation than was shown for calculations at longer timescales (Daloz et al.~~

620 ~~2018), so we suspect that the reanalysis is challenged more in capturing the coupling between the~~
621 ~~radiation and precipitation for shorter timescale variability.~~▲

Formatted: Font:

622 How coupled CIPs are linked with their environment is also examined. Generally, the
623 reanalyses show less heating of the atmosphere at high SSTs and more cooling of the atmosphere
624 at low SSTs. The dynamic regime appears to act as a switch with weak to strong surface cooling
625 efficiencies and from atmospheric cooling to heating as the regime shifts from ascent to
626 subsidence. The thermodynamic regime acts more as a control on the strength of the coupling
627 parameters, especially for R_h . In ascent regimes, precipitating clouds go from weak to strong R_h
628 with increasing SST and CWV which suggests that cloud heat the atmosphere more efficiently
629 per unit rainfall in warm and moist environments. Joint distributions of R_h as a function of SST
630 and CWV in the observations indicate that CWV is the primary control, with relatively constant
631 R_h across a range of SSTs (like 302-305K) for fixed CWV. Reanalyses capture the general
632 relationships between coupled CIPs and their environment, with several important distinctions.
633 Neither ERA-Interim or MERRA-2 capture the strong cooling efficiencies at high SST and
634 CWV, instead they have strong R_c from low to moderate SST and CWV which rapidly weakens
635 at high SST and CWV suggesting that the coupling between precipitation and shortwave cloud
636 forcing in these regimes is too weak in the reanalyses. Likewise, reanalyses also fail to capture
637 the strong heating per unit precipitation with increasing SST and CWV. They also do not appear
638 to be as strongly linked with the environmental moisture as the observations.

639 The observational-reanalyses discrepancies shown here could be caused by a variety of
640 factors including differences in the environmental states in which convection occurs in the
641 reanalyses, differences in the timing and location of reanalysis convection (leading to
642 mismatches with the observations at the shorter timescales examined here), or the precipitation-

643 radiation coupling produced by the model parameterizations. There are notable differences in
644 the environments in which the two reanalyses produce convection which may explain some of
645 the differences between the two reanalyses. However, there are still clear differences between the
646 observations and the reanalyses when the observations are composited by the reanalysis
647 environmental states which suggests the latter two factors could play a bigger role. Attempting
648 to correct timing and location mismatches for every precipitating cloud is beyond the scope of
649 this study, but there are clear indications in the literature that suggest the biases of R_c and R_f
650 between the reanalysis and observations may be linked to both uncertainties in the representation
651 of cloudiness and precipitation intensity, as well as how they are coupled in the reanalysis
652 systems. Both Miao et al. (2019) and Hinkelman. (2019) show that in tropical regions, ERA-
653 Interim exhibits considerable underestimation for high-level clouds, which reduces both the SW
654 and LW CRE at TOA. However, MERRA-2 better represents high-level clouds, perhaps even
655 overrepresents, but tends to underestimate the middle and low-level cloudiness. In MERRA-2's
656 case, the biases of R_c and R_f may be mainly due to the excessive convective precipitation
657 intensity over the warm pool region (Bosilovich et al. 2017). Given the lack of middle and low-
658 level cloudiness, there may also be some biases in radiative fluxes due to cloud thickness. In
659 addition to the potential underestimation in high clouds in ERA-Interim, it may overestimate
660 precipitation in both ascending and descending regimes related to the parameterization scheme
661 used in both convective and marine boundary layer clouds (Dolinar et al 2016) and not capturing
662 the cloud entrainment and detrainment rates (Naud et al. 2014). Fortunately, in the latest version
663 ERA-5 (Hersbach et al 2018), representations of mixed phased clouds and parameterization of
664 convection including entrainment and coupling with large-scale circulation are expected to be
665 improved leading better estimates of convective cloudiness, radiation at TOA, and precipitation.

666 ~~The biases of R_e and R_u between the reanalysis and observations are linked to both~~
667 ~~uncertainties in the representation of cloudiness and precipitation intensity in the reanalysis~~
668 ~~systems. Both Miao et al. (2019) and Hinkelman. (2019) show that in tropical regions, ERA-~~
669 ~~Interim exhibits considerable underestimation for high level clouds, which reduces both the SW~~
670 ~~and LW CRF at TOA. However, MERRA 2 better represents high level clouds, perhaps even~~
671 ~~overrepresents, but tends to underestimate the middle and low level cloudiness. In MERRA 2's~~
672 ~~case, the biases of R_e and R_u may be mainly due to the excessive convective precipitation~~
673 ~~intensity over the warm pool region (Bosilovich et al. 2017). Given the lack of middle and low-~~
674 ~~level cloudiness, there may also be some biases in radiative fluxes due to cloud thickness. In~~
675 ~~addition, the potential underestimation in high clouds in ERA Interim, it may overestimate~~
676 ~~precipitation in both ascending and descending regimes related to the parameterization scheme~~
677 ~~used in both convective and marine boundary layer clouds (Dolinar et al 2016) and not capturing~~
678 ~~the cloud entrainment and detrainment rates (Naud et al. 2014). Fortunately, in the latest version~~
679 ~~ERA 5 (Hersbach et al 2018), representations of mixed phased clouds and parameterization of~~
680 ~~convection including entrainment and coupling with large scale are expected to be improved~~
681 ~~leading better estimates of convective cloudiness, radiation at TOA, and precipitation.~~

682 ~~Observation data inevitably have some uncertainties caused by the retrieval algorithm.~~
683 ~~For instance, 2BFLX partly overcomes the uncertainties in the radiative effects caused by low~~
684 ~~clouds, cirrus and aerosols, but some uncertainties remain in the SW and LW fluxes. The former~~
685 ~~is primarily the result of uncertainties in LWC estimates, and the latter is linked to errors in~~
686 ~~prescribed skin temperature and the lower tropospheric water vapor (Henderson et al. 2013).~~
687 ~~These uncertainties should be considered when comparing observational results and model~~

688 ~~outputs. Estimates from different observation systems in the future could help reduce these~~
689 ~~observational uncertainties.~~

690 Even though over most of the globe, R_h and R_c are not large, Daloz et al. (2018) highlight
691 the importance of R_h and R_c in regions such as the west Pacific Ocean and mid-Atlantic. For
692 example, in failing to simulate R_c and R_h over the Indo-Pacific warm pool, reanalysis also does
693 not capture a strong enough of east-west gradient of R_c and R_h over the Pacific as in the A-Train
694 results. However, as the transition of the precipitation gradient over Pacific becomes more
695 pronounced during an ENSO event, the model response to the circulation becomes more
696 sensitive to the latent heating variation (Schumacher et al 2004). Also, a slight change in surface
697 fluxes and tropospheric moistening over the West Pacific Ocean could have significant influence
698 on the propagation of Madden-Julian Oscillation (MJO) that may not be captured in reanalysis or
699 models given the increasingly large biases between reanalyses and observations at shorter
700 coupling timescales. Daloz et al (2018) ~~also suggested~~~~mentioned~~ that R_h can be a good proxy for
701 processes like convective aggregation. Compensating subsidence around m~~More~~ aggregated
702 convection will make the surrounding atmosphere drier and clearer and increase outgoing
703 longwave radiation to the space (Bretherton et al. 2005; Tobin et al. 2012; Bony et al. 2015;
704 Daloz et al 2018). In our observational results, R_h is high over the warm pool area and generally
705 increases in regions of high CWV and SST, which indicates that the atmospheric radiative
706 heating by deep convection increases faster than the precipitation power law scaling with CWV
707 that has been shown in a number of studies (Bretherton et al. 2004, Ahmed and Schumacher
708 2015~~Masunaga and Bony 2018~~). This could imply that cloud systems vary in such a way,
709 perhaps via convective aggregation in moist regions to become more efficient at heating the
710 atmosphere per unit rainfall to maintain global energy balance with the expanding dry regions.

711 In the future, the coupled CIPs can be compared with those in GCMs or cloud resolving
712 models to understand how well models couple precipitation and radiation, what parameterization
713 need to be improved to better capture the coupling and determine more about the underlying
714 physical processes driving the observed relationship between coupled CIPs and their
715 environment.

716

717 **Acknowledgments**

718 We appreciate the helpful comments and suggestions of three anonymous reviewers, and
719 Dr. Schumacher in Department of Atmospheric Sciences, Texas A&M University, which
720 improved this manuscript considerably. This research is supported by NASA energy and water
721 cycle study (NEWS) Grant NNX15AD13G. The CloudSat data were downloaded from the
722 CloudSat processing center (<http://www.cloudsat.cira.colostate.edu/>). The AMSR-E Rainfall
723 Subset collocated with CloudSat track were downloaded from Goddard Earth Science Data and
724 Information Services Center
725 (http://disc.sci.gsfc.nasa.gov/datacollection/AMSRERR_CPR_V002.html). ERA-Interim data
726 were obtained from the European Centre for Medium-Range Weather Forecasts
727 (<http://apps.ecmwf.int/datasets/>). MERRA-2 data were provided by the Goddard Earth Sciences
728 Data and Information Services Center (<https://disc.gsfc.nasa.gov/daac-bin/FTPSubset2.pl>). All
729 datasets used in this analysis are open access.

730 ~~We are appreciated for the three anonymous reviewers, and Dr. Schumacher in~~
731 ~~Department of Atmospheric Sciences, Texas A&M University for their helpful comments and~~
732 ~~suggestions, which improved the initial version of the manuscript considerably. This research is~~
733 ~~supported by NASA energy and water cycle study (NEWS) Grant NNX15AD13G, the CloudSat~~

734 ~~data were downloaded from the CloudSat processing center~~
735 ~~(<http://www.cloudsat.cira.colostate.edu/>). AMSR-E Rainfall Subset, collocated with CloudSat~~
736 ~~track were got from Goddard Earth Science Data and Information Services Center~~
737 ~~(<http://disc.sci.gsfc.nasa.gov/datacollection/AMSRERR-CPR-V002.html>) The ERA Interim~~
738 ~~data were obtained through from the European Centre for Medium Range Weather Forecasts~~
739 ~~(<http://apps.ecmwf.int/datasets/>). MERRA-2 data were also directly provided by the Goddard~~
740 ~~Earth Sciences Data and Information Services Center ([https://disc.gsfc.nasa.gov/daac-](https://disc.gsfc.nasa.gov/daac-bin/FTPSubset2.pl)~~
741 ~~[bin/FTPSubset2.pl](https://disc.gsfc.nasa.gov/daac-bin/FTPSubset2.pl)). All the dataset has open access.~~

742 **References**

- 743 Ahmed, F., and C. Schumacher, 2015: Convective and stratiform components of the
744 precipitation-moisture relationship. *Geophys. Res. Lett.*, 42, 10 453–10 462,
745 doi:10.1002/2015GL066957.
- 746 Ahmed, F., C. Schumacher, Z. Feng, and S. Hagos, 2016: A retrieval of tropical latent heating
747 using the 3D structure of precipitation features. *J. Appl. Meteor. Climatol.*, 55, 1965–
748 1982, <https://doi.org/10.1175/JAMC-D-15-0038.1>.
- 749 Allan, R. P., 2009: Examination of relationships between clear-sky longwave radiation and
750 aspects of the atmospheric hydrological cycle in climate models, reanalyses, and
751 observations. *J. Climate*, 22, 3127–3145, doi:10.1175/2008JCLI2616.1.
- 752 Allan, R. P., 2011: Combining satellite data and models to estimate cloud radiative effect at the
753 surface and in the atmosphere. *Meteor. Appl.*, 18, 324–333
- 754 Andrew, T., P.M.Forster, O. Boucher, N. Bellouin, and A. Jones, 2010: Precipitation, radiative
755 forcing and global temperature change. *Geophys. Res. Lett.*, 37, L14701,
756 doi:10.1029/2010GL043991.

- 757 [Bacmeister, J. T. and Stephens, G.: Spatial statistics of likely convective clouds in CloudSat data,](#)
758 [J. Geophys. Res., 116, D04104, doi:10.1029/2010JD014444, 2011.](#)
- 759 Behrangi, A., M. Lebsock, S. Wong, and B. Lambrigtsen, 2012: On the quantification of oceanic
760 rainfall using spaceborne sensors. *J. Geophys. Res.*, 117, D20105,
761 <https://doi.org/10.1029/2012JD017979>.
- 762 Behrangi, A., Y. Tian, B. H. Lambrigtsen, and G. L. Stephens, 2014b: What does CloudSat
763 reveal about global land precipitation detection by other spaceborne sensors? *Water*
764 *Resour. Res.*, 50, 4893–4905, doi:10.1002/2013WR014566.
- 765 Betts A. K., R. Desjardins, D. Worth, and B. Beckage, 2014: Climate coupling between
766 temperature, humidity, precipitation, and cloud cover over the Canadian Prairies. *J.*
767 *Geophys. Res. Atmos.*, 119, 13 305–13 326, doi:10.1002/2014JD022511.
- 768 Bodas-Salcedo, A., M. J. Webb, M. E. Brooks, M. A. Ringer, K. D. Williams, S. F. Milton,
769 and D. R. Wilson, 2008: Evaluating cloud systems in the Met Office global forecast
770 model using simulated CloudSat radar reflectivities. *J. Geophys. Res.*, 113, D00A13,
771 doi:<https://doi.org/10.1029/2007JD009620>.
- 772 Bony S, Dufresne JL, Le Treui H, Morcrette JJ, Snior C (2004) On dynamic and thermodynamic
773 components of cloud changes. *Clim Dyn* 22:71–86. doi:10.1007/s00382-003-0369-6
- 774 Bony S, and Coauthors, 2015: Clouds, circulation and climate sensitivity. *Nat. Geosci.*, 8, 261–
775 268, doi:<https://doi.org/10.1038/ngeo2398>.
- 776 Bony S, and J. Dufresne, 2005: Marine boundary layer clouds at the heart of tropical cloud
777 feedback uncertainties in climate models. *Geophys. Res.*
778 *Let.*, 32, L20806, <https://doi.org/10.1029/2005GL023851>.

- 779 Bosilovich, M. G., and Coauthors, 2015b: MERRA-2: Initial evaluation of the climate.
780 NASA/TM-2015-104606, Vol. 43, 139 pp.
- 781 Bosilovich, M. G., R. Lucchesi, and M. Suarez, 2016: MERRA-2: File specification. GMAO
782 Office Note 9, 73 pp. [Available online at
783 <https://gmao.gsfc.nasa.gov/pubs/docs/Bosilovich785.pdf>.]
- 784 Bosilovich, M. G., F. Robertson, L. Takacs, A. Molod, and D. Mocko, 2017: Atmospheric water
785 balance and variability in the MERRA-2 reanalysis. *J. Climate*, 30, 1177–1196,
786 doi:<https://doi.org/10.1175/JCLI-D-16-0338.1>.
- 787 Bouniol, D., R. Roca, T. Fiolleau, and E. Poan, 2016: Macrophysical, microphysical, and
788 radiative properties of tropical mesoscale convective systems along their life cycle. *J.*
789 *Climate*, 29, 3353–3371, doi:10.1175/JCLI-D-15-0551.1.
- 790 Bretherton, C.S. and A.H. Sobel, 2002: A Simple Model of a Convectively Coupled Walker
791 Circulation Using the Weak Temperature Gradient Approximation. *J. Climate*, 15,2907–
792 2920, [https://doi.org/10.1175/1520-0442\(2002\)015<2907:ASMOAC>2.0.CO;2](https://doi.org/10.1175/1520-0442(2002)015<2907:ASMOAC>2.0.CO;2)
- 793 Bretherton, C.S., C. S., M. E. Peters, and L. E. Back, 2004: Relationships between water vapor
794 path and precipitation over the tropical oceans. *J. Climate*, 17, 1517–1528.
- 795 Bretherton, C.S., P. N. Blossey, and M. Khairoutdinov, 2005: An energy-balance analysis of
796 deep convective self-aggregation above uniform SST. *J. Atmos. Sci.*, 62, 4273–
797 4292, <https://doi.org/10.1175/JAS3614.1>.
- 798 Calisto, M., D. Folini, M. Wild, and L. Bengtsson, 2014: Cloud radiative forcing
799 intercomparison between fully coupled CMIP5 models and CERES satellite data. *Ann.*
800 *Geophys.*, 32, 793–807, doi:10.5194/angeo-32-793-2014.

801 Ceppi, P., F. Brient, M. D. Zelinka, and D. L. Hartmann, 2017: Cloud feedback mechanisms and
802 their representation in global climate models. *Wiley Interdiscip. Rev.: Climate Change*, 8,
803 e465, <https://doi.org/10.1002/wcc.465>.

Choi, Y.-S., C.-H. Ho, C.-E. Park, T. Storelvmo, and I. Tan, 2014: Influence of cloud
phase composition on climate feedbacks. *J. Geophys. Res. Atmos.*, 119, 3687–
3700, doi: <https://doi.org/10.1002/2013JD020582>

Clark A.J., W.A.Gallus Jr., and T.-C. Chen (2007) Comparison of the Diurnal
Precipitation Cycle in Convection-Resolving and Non-Convection-Resolving
Mesoscale Models. *Mon. Wea. Rev.*, 135, 3456–
3473, <https://doi.org/10.1175/MWR3467.1>

Colman, R. A., 2015: Climate radiative feedbacks and adjustments at the Earth's surface.
J. Geophys. Res. Atmos., 120, 3173– 3182, doi:10.1002/2014JD022896.

Cullather, R. I., S. M. J. Nowicki, B. Zhao, and M. J. Suarez, 2014: Evaluation of the
surface representation of the Greenland ice sheet in a general circulation model. *J.*
Climate, 27, 4835–4856, <https://doi.org/10.1175/JCLI-D-13-00635.1>.

Dai, A., and K. E. Trenberth, 2004: The diurnal cycle and its depiction in the Community
Climate System Model. *J. Climate*, 17, 930–951, [https://doi.org/10.1175/1520-0442\(2004\)017<0930:TDCAID>2.0.CO;2](https://doi.org/10.1175/1520-0442(2004)017<0930:TDCAID>2.0.CO;2).

Dai, F., R. Yu, X. Zhang, Y. Yu, and J. Li, 2003: The impact of low-level cloud over the
eastern subtropical Pacific on the “double ITCZ” in LASG FGCM-0. *Adv. Atmos.*
Sci., 20, 461–474, doi:<https://doi.org/10.1007/BF02690804>.

Daloz, A., E. Nelson, T. L'Ecuyer, A. Rapp, and L. Sun, 2018: Assessing the coupled

influences of clouds on the Atmospheric Energy and Water Cycles in Reanalyses with A-Train Observations. *J. Climate*. doi:10.1175/JCLI-D-17-0862.1.

Dee D. P., Uppala S. M., Simmons A. J., Berrisford P., Poli P., Kobayashi S., Andrae U., Balmaseda M. A., Balsamo G., Bauer P., Bechtold P., Beljaars A. C. M., van de Berg L., Bidlot J., Bormann N., Delsol C., Dragani R., Fuentes M., Geer A. J., Haimberger L., Healy S. B., Hersbach H., Hólm E. V., Isaksen I., Kållberg P., Köhler M., Matricardi M., McNally A. P., Monge-Sanz B. M., Morcrette J.-J., Park B.-K., Peubey C., de Rosnay P., Tavolato C., Thépaut J.-N. and Vitart, F. (2011) The ERA-Interim reanalysis: configuration and performance of the data assimilation system. *Q.J.R. Meteorol. Soc.*, 137: 553–597. doi: 10.1002/qj.828

804 Dessler, A. E., 2010: A determination of the cloud feedback from climate variations over the past
805 decade. *Science*, 330, 1523–1527, doi:10.1126/science.1192546

806 Dinh, T. and S. Fueglistaler, 2017: Mechanism of fast atmospheric energetic equilibration
807 following radiative forcing by CO₂. *J. Adv. Model. Earth Syst.*, 9, 2468–2482. doi:
808 <https://doi.org/10.1002/2017MS001116>

809 Dolinar E.K., Dong X. and Xi B. (2016): Evaluation and Intercomparison of clouds, precipitation
810 and radiation budgets in recent reanalyses using satellite-surface observations. *Clim.*
811 *Dyn.* 46:2123-2144. doi: 10.1007/s00382-015-2693-z.

812 Eitzen, Z., K. Xu, and T. Wong, 2011: An estimate of low-cloud feedbacks from variations of
813 cloud radiative and physical properties with sea surface temperature on interannual time
814 scales. *J. Climate*, 24, 1106–1121, doi:<https://doi.org/10.1175/2010JCLI3670.1>.

815 Gelaro, R., W. McCarty, M.J. Suárez, R. Todling, A. Molod, L. Takacs, C.A. Randles, A.
816 Darmenov, M.G. Bosilovich, R. Reichle, K. Wargan, L. Coy, R. Cullather, C. Draper, S.

817 Akella, V. Buchard, A. Conaty, A.M. da Silva, W. Gu, G. Kim, R. Koster, R. Lucchesi,
818 D. Merkova, J.E. Nielsen, G. Partyka, S. Pawson, W. Putman, M. Rienecker, S.D.
819 Schubert, M. Sienkiewicz, and B. Zhao, 2017: The Modern-Era Retrospective Analysis
820 for Research and Applications, Version 2 (MERRA-2). *J. Climate*, 30, 5419–
821 5454, <https://doi.org/10.1175/JCLI-D-16-0758.1>

822 Global Hydrology Resource Center/MSFC/NASA (2009), AMSR-E L2 Rainfall Subset,
823 collocated with CloudSat track V002, Edited by GES DISC, Greenbelt, MD, USA,
824 Goddard Earth Sciences Data and Information Services Center (GES DISC), Accessee:
825 09-01-2017, https://disc.gsfc.nasa.gov/datacollection/AMSRERR_CPR_002.html

826 Grabowski, W. W., Bechtold, P., Cheng, A., Forbes, R., Halliwell, C., Khairoutdinov, M., Lang,
827 S., Nasuno, T., Petch, J., Tao, W.-K., Wong, R., Wu, X. and Xu, K.-M. (2006), Daytime
828 convective development over land: A model intercomparison based on LBA
829 observations. *Q.J.R. Meteorol. Soc.*, 132: 317–344. doi:10.1256/qj.04.147

830 Griggs, J., and J. Bamber, 2008: Assessment of cloud cover characteristics in satellite datasets
831 and reanalysis products for Greenland. *J. Climate*, **21**, 1837–1849.

832 Haynes, J. M., and G. L. Stephens (2007), Tropical oceanic cloudiness and the incidence of
833 precipitation: Early results from CloudSat, *Geophys. Res. Lett.*, 34, L09811,
834 doi:10.1029/2007GL029335.

835 Haynes, J. M., T. S. L'Ecuyer, G. L. Stephens, S. D. Miller, C. Mitrescu, N. B. Wood, and S.
836 Tanelli, 2009: Rainfall retrieval over the ocean with spaceborne W-band radar. *J.*
837 *Geophys. Res.*, 114, D00A22, doi:10.1029/2008JD009973.

838 Held, I. M., and B. J. Soden, 2006: Robust responses of the hydrological cycle to global
839 warming. *J. Climate*, 19, 5686–5699, <https://doi.org/10.1175/JCLI3990.1>.

- 840 Henderson, D.S., T. L'Ecuyer, G. Stephens, P. Partain, and M. Sekiguchi, 2013: A Multisensor
841 Perspective on the Radiative Impacts of Clouds and Aerosols. *J. Appl. Meteor.*
842 *Climatol.*, 52, 853–871, doi:10.1175/JAMC-D-12-025.1.
- 843 Hersbach, H., P. de Rosnay, B. Bell, D. Schepers, A. Simmons, C. Soci, S. Abdalla, M. Alonso
844 Balmaseda, G. Balsamo, P. Bechtold, P. Berrisford, J. Bidlot, E. de Boisséson, M.
845 Bonavita, P. Browne, R. Buizza, P. Dahlgren, D. Dee, R. Dragani, M. Diamantakis, J.
846 Flemming, R. Forbes, A. Geer, T. Haiden, E. Hólm, L. Haimberger, R. Hogan, A.
847 Horányi, M. Janisková, P. Laloyaux, P. Lopez, J. Muñoz-Sabater, C. Peubey, R. Radu, D.
848 Richardson, J.-N. Thépaut, F. Vitart, X. Yang, E. Zsótér & H. Zuo, 2018: Operational
849 global reanalysis: progress, future directions and synergies with NWP, ECMWF ERA
850 Report Series 27
- 851 Hinkelman, L.M., 2019: The Global Radiative Energy Budget in MERRA and MERRA-2:
852 Evaluation with Respect to CERES EBAF Data. *J. Climate*, 32, 197301994,
853 <https://doi.org/10.1175/JCLI-D-18-0445.1>
- 854 Holloway, C. E., and J. D. Neelin, 2009: Moisture vertical structure, column water vapor, and
855 tropical deep convection. *J. Atmos. Sci.*, 66, 1665–1683, doi:10.1175/2008JAS2806.1.
- 856 Huaman, L., C. Schumacher, 2017: Assessing the vertical latent heating structure of the East
857 Pacific ITCZ using the CloudSat CPR and TRMM CPR. *J. Climate*, 31, 2563-2577, doi:
858 10.1175/JCLI-D-17-0590.1
- 859 Itterly, K. F., and P. C. Taylor, 2014: Evaluation of the tropical TOA flux diurnal cycle in
860 MERRA and ERA-Interim retrospective analyses. *J. Climate*, 27, 4781–4796,
861 doi:10.1175/JCLI-D-13-00737.1.

- 862 Jakob, C. and Klein, S. A. (2000), A parametrization of the effects of cloud and precipitation
863 overlap for use in general-circulation models. *Q.J.R. Meteorol. Soc.*, 126: 2525–2544.
864 doi:10.1002/qj.49712656809
- 865 Jakob, C., and G. Tselioudis, 2003: Objective identification of cloud regimes in the tropical
866 western Pacific. *Geophys. Res. Lett.*, 30, 2082, doi:10.1029/2003GL018367.
- 867 Jakob, C., G. Tselioudis, and T. Hume, 2005: The radiative, cloud, and thermodynamic
868 properties of the major tropical western Pacific cloud regimes. *J. Climate*, 18, 1203–
869 1215.
- 870 Kay, J., and Coauthors, 2012: Exposing global cloud biases in the Community Atmosphere
871 Model (CAM) using satellite observations and their corresponding instrument
872 simulators. *J. Climate*, 25, 5190–5207, doi:<https://doi.org/10.1175/JCLI-D-11-00469.1>.
- 873 Kim, D., M.-S. Ahn, I.-S. Kang, and A. D. Del Genio, 2015: Role of longwave cloud–radiation
874 feedback in the simulation of the Madden–Julian oscillation. *J. Climate*, 28, 6979–6994,
875 doi:10.1175/JCLI-D-14-00767.1.
- 876 Kim, J. and M.J. Alexander, 2013: Tropical Precipitation Variability and Convectively Coupled
877 Equatorial Waves on Sub-monthly Time Scales in Reanalyses and TRMM. *J.*
878 *Climate*, 26, 3013–3030, <https://doi.org/10.1175/JCLI-D-12-00353.1>
- 879 Klein, S. A., and D. L. Hartmann, 1993: The seasonal cycle of low stratiform clouds. *J.*
880 *Climate*, 6, 1587–1606, doi:[https://doi.org/10.1175/1520-](https://doi.org/10.1175/1520-0442(1993)006<1587:TSCOLS>2.0.CO;2)
881 [0442\(1993\)006<1587:TSCOLS>2.0.CO;2](https://doi.org/10.1175/1520-0442(1993)006<1587:TSCOLS>2.0.CO;2).
- 882 Kohler M., Ahlgrimm M., Beljaars A.C.M. (2011) Unified treatment of dry convective and
883 stratocumulus-topped boundary layers in the ECMWF model. *Q.J.R. Meteo. Sci.* 137:43-
884 57.

- 885 Kubar, T. L., D. E. Waliser, J. L. Li, and X. Jiang, 2012: On the annual cycle, variability, and
886 correlations of oceanic lowtopped clouds with large-scale circulation using Aqua MODIS
887 and ERA-Interim. *J. Climate*, 25, 6152–6174, doi:10.1175/JCLI-D-11-00478.1.
- 888 Kummerow, C. D., S. Ringerud, J. Crook, D. Randel, and W. Berg, 2011: An observationally
889 generated a priori database for microwave rainfall retrievals. *J. Atmos. Oceanic Technol.*,
890 28, 113–130, doi:10.1175/2010JTECHA1468.1.
- 891 Kummerow, C. D., D. L. Randel, M. Kulie, N-Y. Wang, R. Ferraro, S. J. Munchak, and V.
892 Petkovic, 2015: The evolution of the Goddard profiling algorithm to a fully parametric
893 scheme. *J. Atmos. Oceanic Technol.*, doi:10.1175/JTECH-D-15-0039.1
- 894 Larson, K., and D. L. Hartmann and S. A. Klein, 1999: The role of clouds, water vapor,
895 circulation, and boundary layer structure in the sensitivity of the tropical climate. *J.*
896 *Climate*, 12, 2359–2374.
- 897 Larson, K., and D. L. Hartmann, 2003: Interactions among cloud, water vapor, radiation, and
898 large-scale circulation in the tropical climate. Part I: Sensitivity to uniform sea surface
899 temperature changes. *J. Climate*, 16, 1425–1440.
- 900 Larson, K., and D. L. Hartmann, 2003: Interactions among cloud, water vapor, radiation, and
901 large-scale circulation in the tropical climate. Part II: Sensitivity to spatial gradients of
902 sea surface temperature. *J. Climate*, 16, 1441–1455.
- 903 Lee, M.-I., I.-S. Kang, J.-K. Kim, and B. E. Mapes, 2001: Influence of cloud-radiation
904 interaction on simulating tropical intraseasonal oscillation with an atmospheric general
905 circulation model. *J. Geophys. Res.* 106, 14219–14233.
- 906 Lebsock, M. D., and T. S. L'Ecuyer, 2011: The retrieval of warm rain from CloudSat. *J.*
907 *Geophys. Res.*, 116, D20209, <https://doi.org/10.1029/2011JD016076>.

- 908 Lebrock, M. D., and T. S. L'Ecuyer, D. Vane, G. Stephens, and D. Reinke, 2011: Level 2C
909 RAIN-PROFILE product process description and interface control document, algorithm
910 version 0.0. JPL Rep., 14
911 pp., [http://www.cloudsat.cira.colostate.edu/sites/default/files/products/files/2C-RAIN-](http://www.cloudsat.cira.colostate.edu/sites/default/files/products/files/2C-RAIN-PROFILE-PDICD.P_R04.20110620.pdf)
912 [PROFILE-PDICD.P_R04.20110620.pdf](http://www.cloudsat.cira.colostate.edu/sites/default/files/products/files/2C-RAIN-PROFILE-PDICD.P_R04.20110620.pdf).
- 913 Level 2B Fluxes and Heating Rates and 2B Fluxes and Heating Rates w/ Lidar Process
914 Description and Interface Control Document, CloudSat Team, 2006.
- 915 L'Ecuyer, T. S., H. Masunaga, and C. Kummerow, 2006: Variability in the characteristics of
916 precipitation systems in the tropical Pacific. Part II: Implications for atmospheric
917 heating. *J. Climate*, 19, 1388–1406.
- 918 L'Ecuyer, T. S., and G. L. Stephens, 2007: The Tropical Atmospheric Energy Budget from the
919 TRMM Perspective. Part II: Evaluating GCM Representations of the Sensitivity of
920 Regional Energy and Water Cycles to the 1998-99 ENSO Cycle, *J. Climate* 20, 4548-
921 4571.
- 922 L'Ecuyer, T. S., N.B. Wood, T. Haladay, G.L. Stephens, and P.W. Stackhouse Jr., 2008: Impact
923 of clouds on atmospheric heating based on the R04 CloudSat fluxes and heating rates
924 dataset. *J. Geophys. Res.*, 113, D00A15, doi:10.1029/2008JD009951.
- 925 L'Ecuyer, T. S., and J.H. Jiang, 2010: Touring the atmosphere aboard the A-Train. *Phys.*
926 *Today*, 63, 36–41, doi:10.1063/1.3463626.
- 927 Li, J. L., X. H. Zhang, Y. Q. Yu, and F. S. Dai, 2004: Primary reasoning behind the double ITCZ
928 phenomenon in a coupled ocean-atmosphere general circulation model. *Adv. Atmos.*
929 *Sci.*, 21, 857–867, doi:<https://doi.org/10.1007/BF02915588>.

930 Liu, Y., and J. R. Key, 2016: Assessment of Arctic cloud cover anomalies in atmospheric
931 reanalysis products using satellite data. *J. Climate*, **29**, 6065–
932 6083, <https://doi.org/10.1175/JCLI-D-15-0861.1>.

933 Liu, Y., and Q. Zhang, 2014: The CloudSat radar–lidar geometrical profile product (RL-
934 GeoProf): Updates, improvements, and selected results. *J. Geophys. Res.*
935 *Atmos.*, 119, 9441–9462, doi:<https://doi.org/10.1002/2013JD021374>.

936 Mace, G. G., and S. Benson, 2017: Diagnosing cloud microphysical process information from
937 remote sensing measurements—A feasibility study using aircraft data. Part I: Tropical
938 anvils measured during TC4. *J. Appl. Meteor. Climatol.*, 56, 633–649,
939 doi:<https://doi.org/10.1175/JAMC-D-16-0083.1>.

940 Mace, G. G., and Q. Zhang, 2014: The CloudSat radar–lidar geometrical profile product (RL-
941 GeoProf): Updates, improvements, and selected results. *J. Geophys. Res. Atmos.*, 119,
942 9441–9462, doi:10.1002/2013JD021374.

943 Mace, G. G., Q. Zhang, M. Vaughan, R. Marchand, G. Stephens, C. Trepte, and D. Winker,
944 2009: A description of hydrometeor layer occurrence statistics derived from the first year
945 of merged CloudSat and CALIPSO data. *J. Geophys. Res.*, 114, D00A26,
946 doi:10.1029/2007JD009755.

947 Masunaga, H., and T. S. L'Ecuyer, 2011: Equatorial asymmetry of the east Pacific ITCZ:
948 Observational constraints on the underlying processes. *J. Climate*, 24, 1784–1800,
949 doi:<https://doi.org/10.1175/2010JCLI3854.1>.

950 ~~Masunaga, H., and S. Bony, 2018: Radiative Invigoration of Tropical Convection by Preceding~~
951 ~~Cirrus Clouds. *J. Atmos. Sci.*, 75, 1327–1342, <https://doi.org/10.1175/JAS-D-17-0355.1>~~

- 952 Miao, H, Wang, X, Liu, Y, Wu, G. An evaluation of cloud vertical structure in three reanalyses
953 against CloudSat/cloud-aerosol lidar and infrared pathfinder satellite observations. *Atmos*
954 *Sci Lett.* 2019; 20:e906. <https://doi.org/10.1002/asl.906>
- 955 Mlawer E.J., Taubman S.J., Brown P.D., Iacono M.J., Clough S.A. (1997) Radiative transfer for
956 inhomogeneous atmospheres: RRTM, a validated correlated-k model for the longwave. *J.*
957 *Geophys. Res.* 102D:16663-16682.
- 958 Molod A., L. Takacs, M.Suarez and J. Bacmeister, 2015: Development of the GEOS-5 general
959 circulation model: evolution from MERRA to MERRA2. *Geosc. Model. Ev.*, 8, 1339-
960 1356.
- 961 Moorthi, S., and M. J. Suarez, 1992: Relaxed Arakawa–Schubert: A parameterization of moist
962 convection for general circulation models. *Mon. Wea. Rev.*, 120, 978–1002,
963 doi:[https://doi.org/10.1175/1520-0493\(1992\)120<0978:RASAPO>2.0.CO;2](https://doi.org/10.1175/1520-0493(1992)120<0978:RASAPO>2.0.CO;2).
- 964 Muller, C. J., and I. M. Held, 2012: Detailed investigation of the self-aggregation of convection
965 in cloud-resolving simulations. *J. Atmos. Sci.*, 69, 2551–
966 2565, <https://doi.org/10.1175/JAS-D-11-0257.1>.
- 967 Muller, C. J., and S. Bony, 2015: What favors convective aggregation and why? *Geophys. Res.*
968 *Lett.*, 42, 5626–5634, doi:10.1002/2015GL064260.
- 969 Naud, C. M., J. F. Booth, and A. D. Del Genio, 2014: Evaluation of ERA-Interim and MERRA
970 cloudiness in the Southern Ocean. *J. Climate*, 27, 2109–
971 2124, <https://doi.org/10.1175/JCLI-D-13-00432.1>.
- 972 Neelin, J. D., O. Peters, and K. Hales, 2009: The transition to strong convection. *J. Atmos. Sci.*,
973 66, 2367–2384, doi:10.1175/2009JAS2962.1.

- 974 Nguyen, H., A. Evans, C. Lucas, I. Smith, and B. Timbal, 2013: The Hadley circulation in
975 reanalyses: Climatology, variability, and change. *J. Climate*, 26, 3357–3376,
976 <https://doi.org/10.1175/JCLI-D-12-00224.1>.
- 977 O’Brien, T. A., F. Li, W. D. Collins, S. A. Rauscher, T. D. Ringler, M. A. Taylor, S. M. Hagos,
978 and L. R. Leung, 2013: Observed scaling in clouds and precipitation and scale
979 incognizance in regional to global atmospheric models. *J. Climate*, 26, 9313– 9333,
980 [doi:10.1175/JCLI-D-13-00005.1](https://doi.org/10.1175/JCLI-D-13-00005.1).
- 981 O’Gorman, P. A., R. P. Allan, M. P. Byrne, and M. Previdi, 2012: Energetic constraints on
982 precipitation under climate change. *Surv. Geophys.*, 33, 585–608, [doi:10.1007/s10712-](https://doi.org/10.1007/s10712-011-9159-6)
983 [011-9159-6](https://doi.org/10.1007/s10712-011-9159-6).
- 984 Pendergrass, A. G., and D. L. Hartmann, 2014: The atmospheric energy constraint on global-
985 mean precipitation change. *J. Climate*, 27, 757–768, [doi:https://doi.org/10.1175/JCLI-D-](https://doi.org/10.1175/JCLI-D-13-00163.1)
986 [13-00163.1](https://doi.org/10.1175/JCLI-D-13-00163.1).
- 987 Peters, O., and J. D. Neelin, 2006: Critical phenomena in atmospheric precipitation. *Nat. Phys.*,
988 2, 393–396.
- 989 Previdi, M., 2010: Radiative feedbacks on global precipitation. *Environ. Res. Lett.*, 5, 025211,
990 [doi:10.1088/1748-9326/5/2/025211](https://doi.org/10.1088/1748-9326/5/2/025211).
- 991 Rädel, G., T. Mauritsen, B. Stevens, D. Dommenges, D. Matei, K. Bellomo, and A. Clement,
992 2016: Amplification of El Niño by cloud longwave coupling to atmospheric circulation.
993 *Nat. Geosci.*, 9, 106–110, <https://doi.org/10.1038/ngeo2630>.
- 994 Randall, D. and Coauthors, 2007: Climate models and their evaluation. *Climate Change 2007:*
995 *The Physical Science Basis. Contribution of Working Group I to the Fourth Assessment*
996 *Report of the Intergovernmental Panel on Climate Change*, S. Solomon, D. Qin, M.

- 997 Manning, Z. Chen, M. Marquis, K. Averyt, M. Tignor, and H. Miller, Eds., Cambridge
998 University Press, Cambridge, 589-662.
- 999 Ritter, B., and J.-F. Geleyn, 1992: A comprehensive radiation scheme for numerical weather
1000 prediction models with potential applications in climate simulations. *Mon. Wea.*
1001 *Rev.*, **120**, 303–325, [https://doi.org/10.1175/1520-](https://doi.org/10.1175/1520-0493(1992)120<0303:ACRSFN>2.0.CO;2)
1002 [0493\(1992\)120<0303:ACRSFN>2.0.CO;2](https://doi.org/10.1175/1520-0493(1992)120<0303:ACRSFN>2.0.CO;2).
- 1003 Schumacher, C., R. A. Houze Jr., and I. Kraucunas, 2004: The tropical dynamical response to
1004 latent heating estimates derived from the TRMM precipitation radar. *J. Atmos. Sci.*, **61**,
1005 1341–1358, [https://doi.org/10.1175/1520-0469\(2004\)061,1341:TTDRTL.2.0.CO;2](https://doi.org/10.1175/1520-0469(2004)061,1341:TTDRTL.2.0.CO;2).
- 1006 Sobel and H. Gildor, 2003: A simple time-dependent model of SST hot spots. *J. Climate*, **16**,
1007 3978–3992.
- 1008 Song, X., and G. Zhang, 2009: Convection parameterization, tropical Pacific double ITCZ, and
1009 upper-ocean biases in the NCAR CCSM3. Part I: Climatology and atmospheric
1010 feedback. *J. Climate*, **22**, 4299–4315, doi:<https://doi.org/10.1175/2009JCLI2642.1>.
- 1011 Stengel, M., Schlundt, C., Stapelberg, S., Sus, O., Eliasson, S., Willén, U., and Meirink, J. F.:
1012 Comparing ERA-Interim clouds with satellite observations using a simplified satellite
1013 simulator, *Atmos. Chem. Phys. Discuss.*, <https://doi.org/10.5194/acp-2018-258>, in
1014 review, 2018
- 1015 Stephens, G., 2005: Cloud feedbacks in the climate system: A critical review. *J. Climate*, **18**,
1016 237–273, doi:[10.1175/JCLI-3243.1](https://doi.org/10.1175/JCLI-3243.1).
- 1017 Stephens, G., and Coauthors, 2008: CloudSat mission: Performance and early science after the
1018 first year of operation. *J. Geophys. Res.*, **113**, D00A18, doi:[10.1029/2008JD009982](https://doi.org/10.1029/2008JD009982).

- 1019 Stephens, G., and T. D. Ellis, 2008: Controls of global-mean precipitation increases in global
1020 warming GCM experiments. *J. Climate*, 21, 6141-6155,
1021 <https://doi.org/10.1175/2008JCLI2144.1>.
- 1022 Stephens, G., and Coauthors, 2010: Dreary state of precipitation in global models. *J. Geophys.*
1023 *Res.*, 115, D24211, doi:10.1029/2010JD014532.
- 1024 Stephens, G., D. Winker, J. Pelon, C. Trepte, D. Vane, C. Yuhas, T. L'Ecuyer, and M.
1025 Lebsock, 2017: CloudSat and CALIPSO within the A-Train: Ten years of actively
1026 observing the Earth system. *Bull. Amer. Meteor. Soc.*, 0, [https://doi.org/10.1175/BAMS-](https://doi.org/10.1175/BAMS-D-16-0324.1)
1027 [D-16-0324.1](https://doi.org/10.1175/BAMS-D-16-0324.1)
- 1028 Sassen, K., Z. Wang, and D. Liu, 2008: The global distribution of cirrus clouds from
1029 CloudSat/Cloud-Aerosol Lidar and Infrared Pathfinder Satellite Observations
1030 (CALIPSO) measurements. *J. Geophys. Res.*, 113, D00A12, doi:10.1029/2008JD009972
- 1031 Stevens, B., and S. Bony, 2013: What are climate models missing? *Science*, 340, 1053–
1032 1054, <https://doi.org/10.1126/science.1237554>.
- 1033 Kociuba, G., and S. B. Power, 2015: Inability of CMIP5 models to simulate recent strengthening
1034 of the Walker circulation: Implications for projections. *J. Climate*, 28, 20–35,
1035 doi:10.1175/JCLI-D-13-00752.1.
- 1036 Tanelli, S., S. L. Durden, E. Im, K. S. Pak, D. G. Reinke, P. Partain, J. M. Haynes, and R. T.
1037 Marchand, 2008: CloudSat's Cloud Profiling Radar after two years in orbit: Performance,
1038 calibration, and processing. *IEEE Trans. Geosci. Remote Sens.*, 46, 3560–3573,
1039 doi:10.1109/TGRS.2008.2002030.

- 1040 Tobin, I., S. Bony, and R. Roca, 2012: Observational evidence for relationships between the
1041 degree of aggregation of deep convection, water vapor, surface fluxes, and radiation. *J.*
1042 *Climate*, 25, 6885–6904, <https://doi.org/10.1175/JCLI-D-11-00258.1>.
- 1043 Trenberth, K. E., J. T. Fasullo, C. O’Dell, and T. Wong, 2010: Relationships between tropical
1044 sea surface temperature and top-of-atmosphere radiation. *Geophys. Res. Lett.*, 37,
1045 L03702, doi:10.1029/2009GL042314.
- 1046 Turk, F. J., and S. D. Miller, 2005: Toward improved characterization of remotely sensed
1047 precipitation regimes with MODIS/ AMSR-E blended data techniques. *IEEE Trans.*
1048 *Geosci. Remote Sens.*, 43, 1059–1069.
- 1049 Voigt, A., and T. A. Shaw, 2015: Circulation response to warming shaped by radiative changes
1050 of clouds and water vapour. *Nat. Geosci.*, 8, 102–106, doi:10.1038/ngeo2345.
- 1051 Waliser, D. E., R. Murtugudde, and L. Lucas, 2003: Indo-Pacific Ocean response to atmospheric
1052 intraseasonal variability. Part I: Austral summer and the Madden-Julian Oscillation. *J.*
1053 *Geophys. Res.*, 108.3160, doi:10.1029/2002JC001620.
- 1054 Wang, S., and A. H. Sobel, 2011: Response of convection to relative sea surface temperature:
1055 Cloud-resolving simulations in two and three dimensions. *J. Geophys.*
1056 *Res.*, 116, D11119, doi:https://doi.org/10.1029/2010JD015347.
- 1057 Wilcox, E. M., and V. Ramanathan, 2001: Scale dependence of the thermodynamic forcing of
1058 tropical monsoon clouds: Results from TRMM observations. *J. Climate*, 14, 1511–1524.
- 1059 Wilheit, T., C. Kummerow, and R. Ferraro, 2003: Rainfall algorithms for AMSR-E. *IEEE Trans.*
1060 *Geosci. Remote Sens.*, 41, 204–214.
- 1061 Wood, R., 2012: Stratocumulus clouds. *Mon. Wea. Rev.*, 140, 2373–2423,
1062 <https://doi.org/10.1175/MWR-D-11-00121.1>.

1063 Xu, K.-M., T. Wong, B. A. Wielicki, L. Parker, and Z. A. Eitzen, 2005: Statistical analyses of
1064 satellite cloud object data from CERES. Part I: Methodology and preliminary results of
1065 1998 El Niño/2000 La Niña. *J. Climate*, 18, 2497–2514,
1066 doi:<https://doi.org/10.1175/JCLI3418.1>.

1067 Xu, K.-M., A. Cheng, and M. Zhang, 2010: Cloud-resolving simulation of low-cloud feedback to
1068 an increase in sea surface temperature. *J. Atmos. Sci.*, 67, 730–748,
1069 doi:<https://doi.org/10.1175/2009JAS3239.1>.

1070 Xu, K.-M., T. Wong, S. Dong, F. Chen, S. Kato, and P. C. Taylor, 2016a: Cloud object analysis
1071 of CERES Aqua observations of tropical and subtropical cloud regimes, Part I: Four-year
1072 climatology. *J. Climate*, 29, 1617–1638, doi:<https://doi.org/10.1175/JCLI-D-14-00836.1>.

1073 Ying, J., and P. Huang, 2016: Cloud–radiation feedback as a leading source of uncertainty in the
1074 tropical Pacific SST warming pattern in CMIP5 models. *J. Climate*, 29, 3867–3881,
1075 doi:[10.1175/JCLI-D-15-0796.1](https://doi.org/10.1175/JCLI-D-15-0796.1).

1076 Zhang, M. H., R. D. Cess, and S. C. Xie, 1996: Relationship between cloud radiative forcing and
1077 sea surface temperatures over the entire tropical oceans. *J. Climate*, 9, 1374–1384,
1078 doi:[10.1175/1520-0442\(1996\)009,1374:RBCRFA.2.0.CO;2](https://doi.org/10.1175/1520-0442(1996)009<1374:RBCRFA.2.0.CO;2).

1079

1080

1081

1082

1083

1084

1085

1086

1087

1088

1089

1090

1091

1092

1093

1094

1095

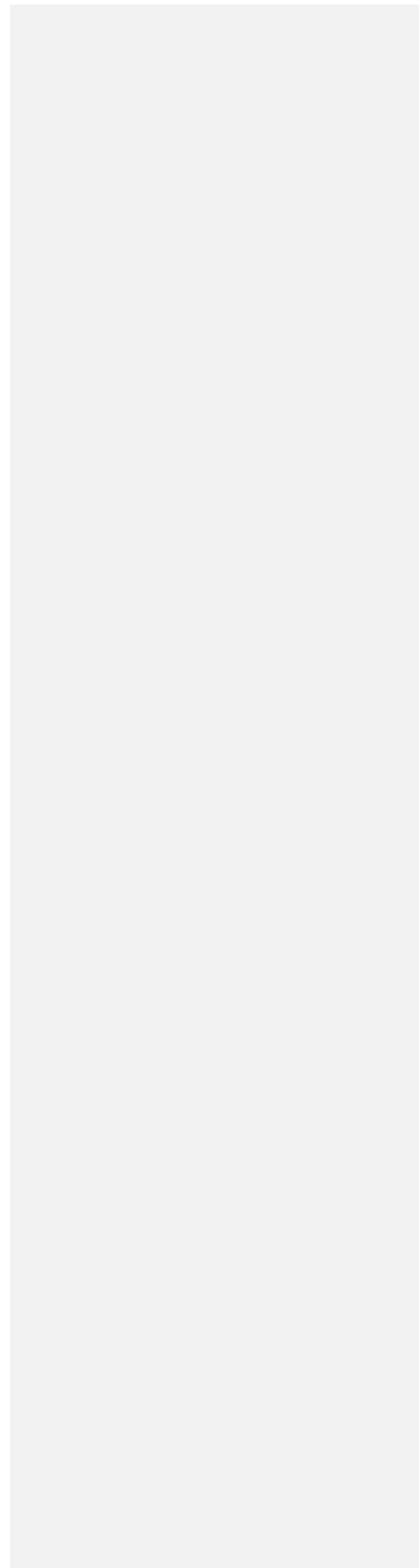
1096

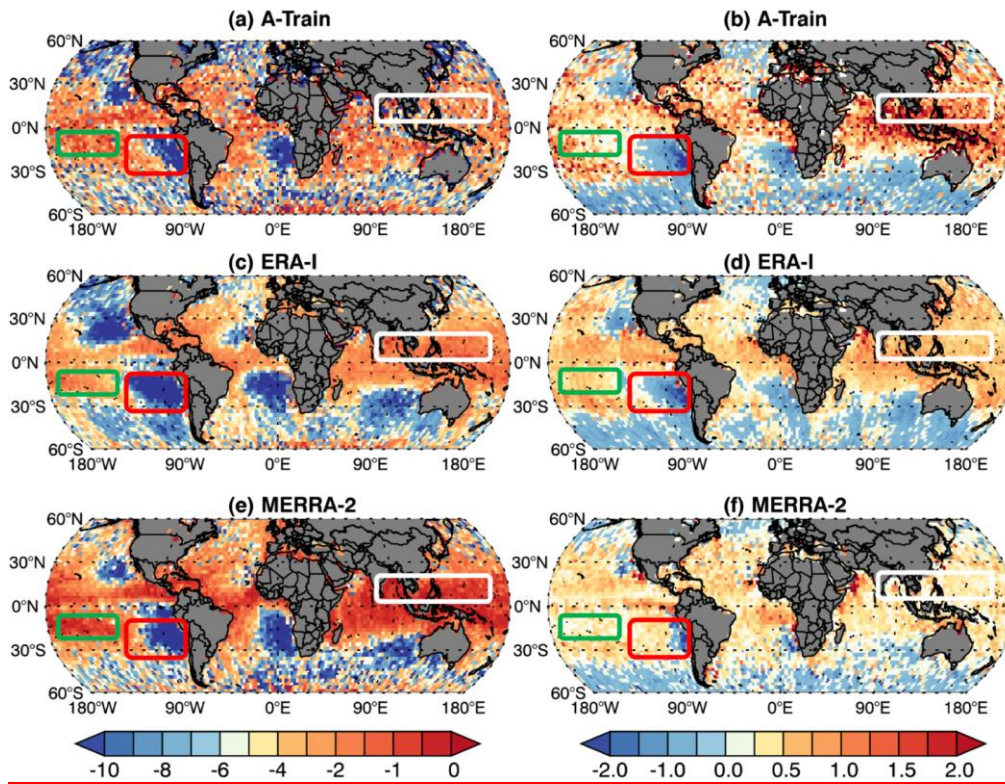
1097

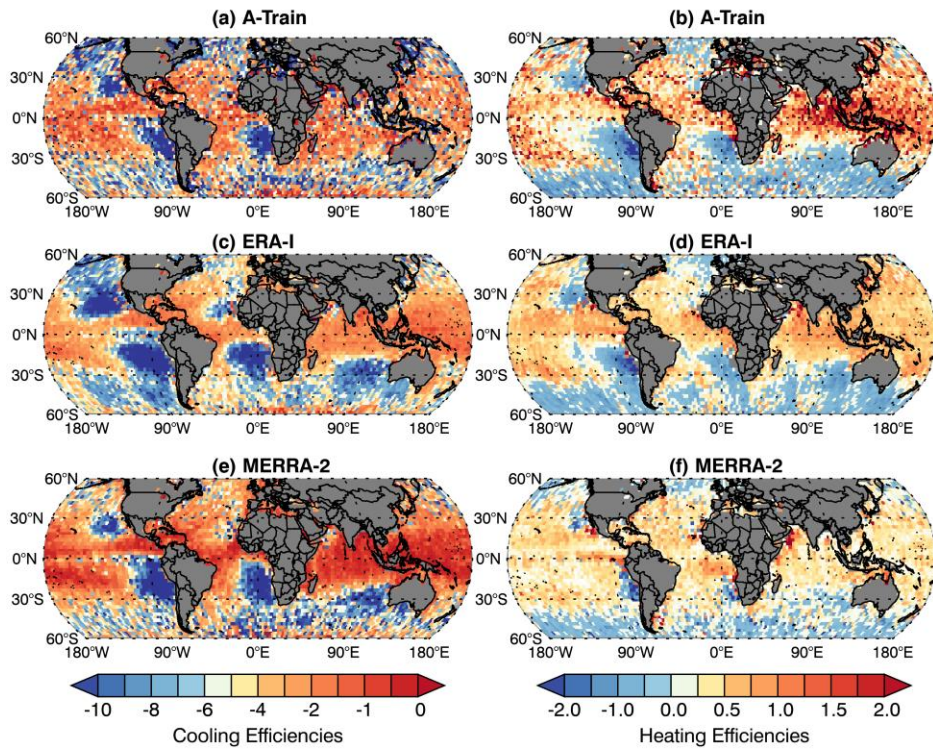
1098

1099

1100 **Figures**







1102
1103 **Figure 1:** The global observed distributions of R_c (a, c, e) and R_h (b, d, e) derived from A-Train

1104 (a, b), ERA-Interim (c, d) and MERRA-2 (e, f) from September 2006 - December 2010

1105

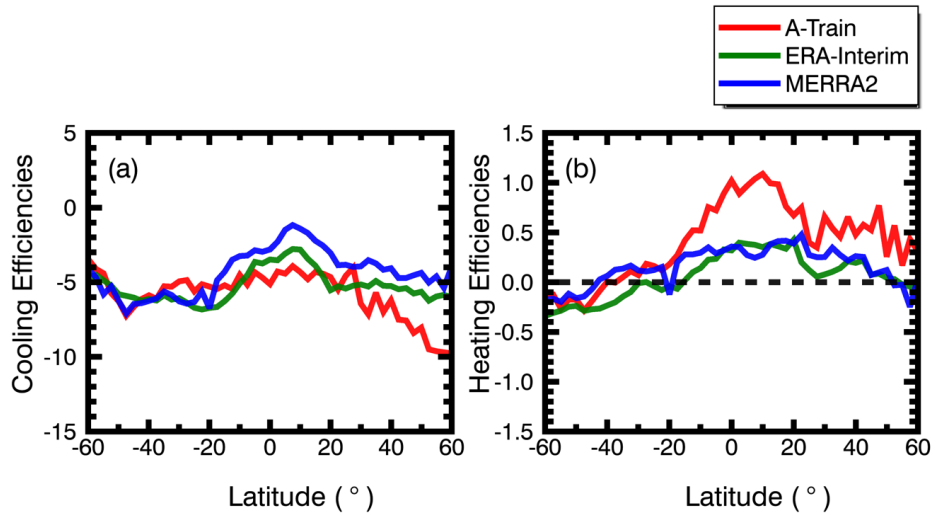
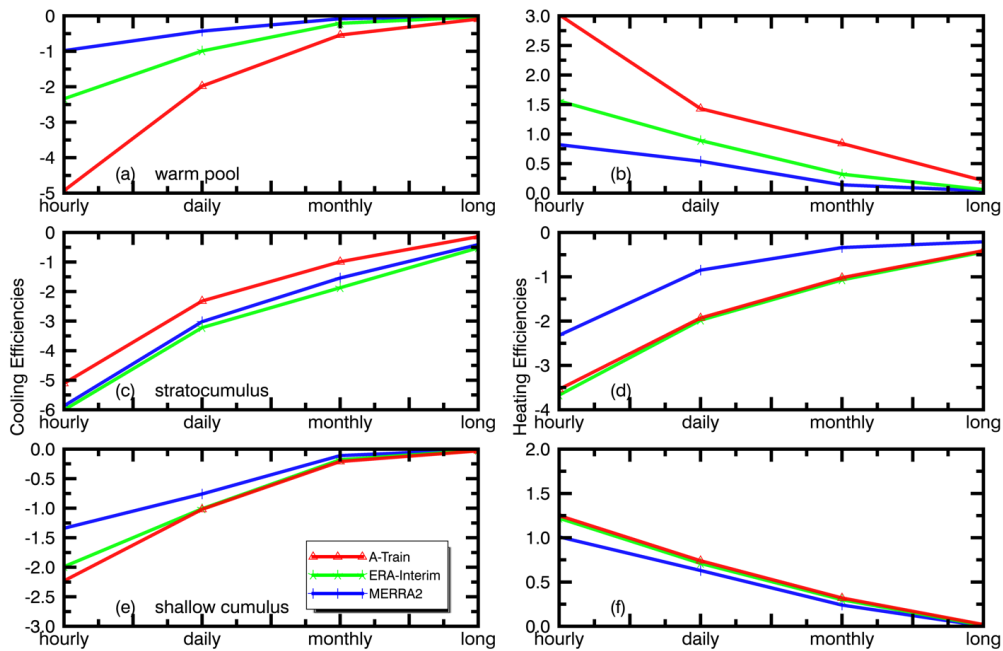


Figure 2: Zonal Mean of (a) R_c and (b) R_h derived from CloudSat, MERRA2 and ERA-Interim from September 2006 to December 2010

Formatted: Centered



1106

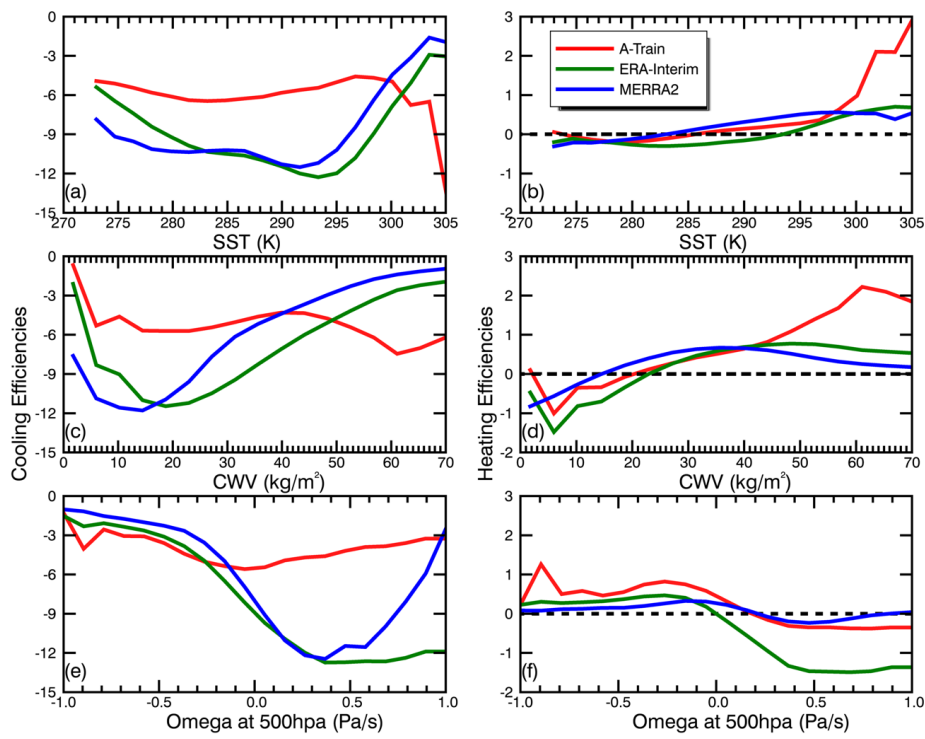
1107

1108

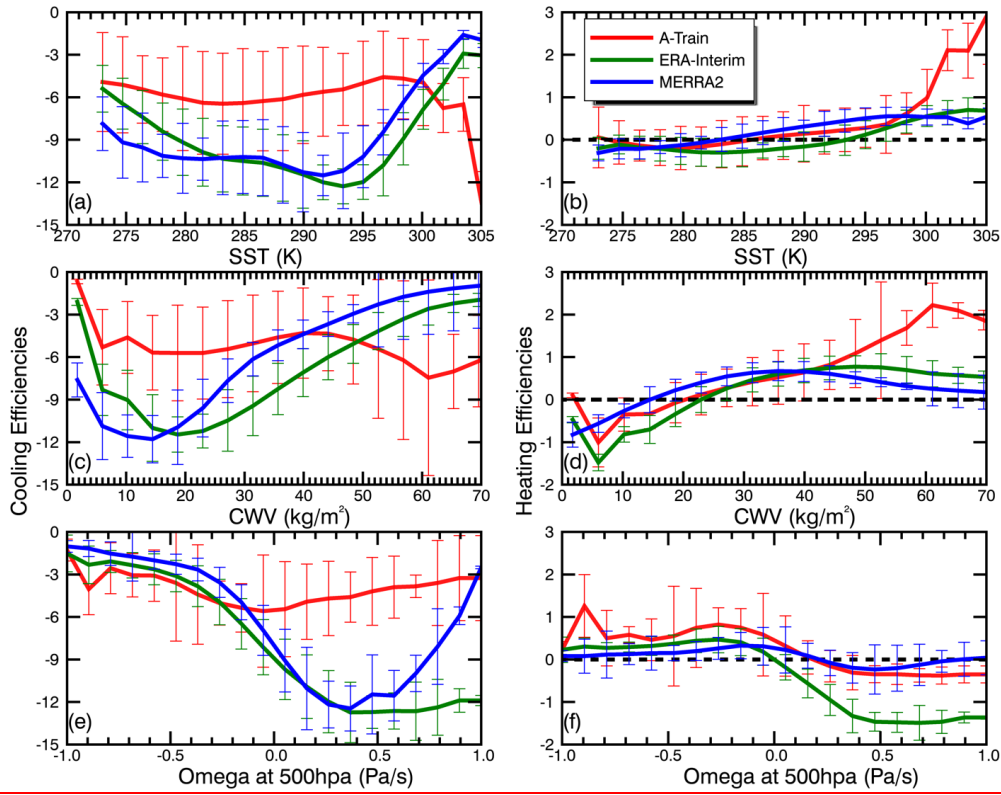
1109

1110

1111 **Figure 2:** Time-scale dependence of both of R_c (left column) and R_h (right column) derived from
 1112 A-Train, ERA-Interim, MERRA-2 for the three cloud regimes highlighted in Figure 1: (a, b)
 1113 warm pool (25°S–15°N, 90–170°E), (c, d) stratocumulus (0–30°S, 70–100°W), and (e, f) shallow
 1114 cumulus (15–30°S, 150–180°W).



1117

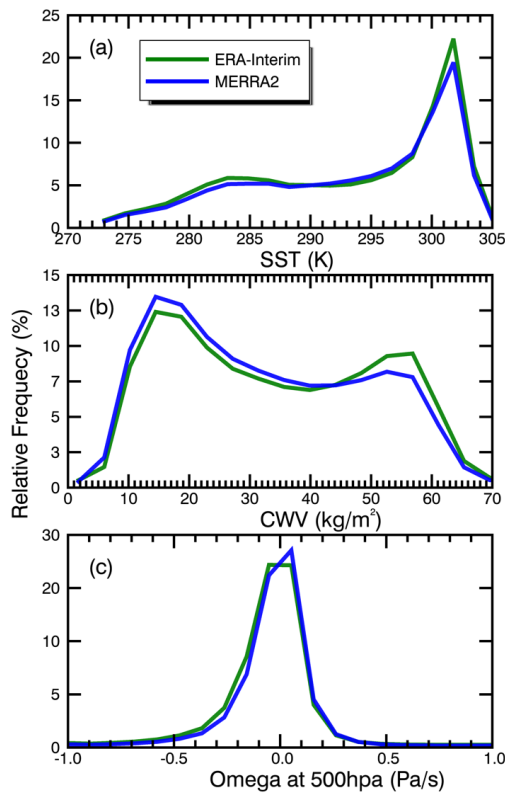


Formatted: Font: 11 pt

1118

1119

Figure 34: (a,c,e) R_c and (b,d,f) R_h as a function of (a,b) SST, (c,d) CWV, and (e,f) ω_{500} .



1120

1121

1122

1123

1124

1125

1126

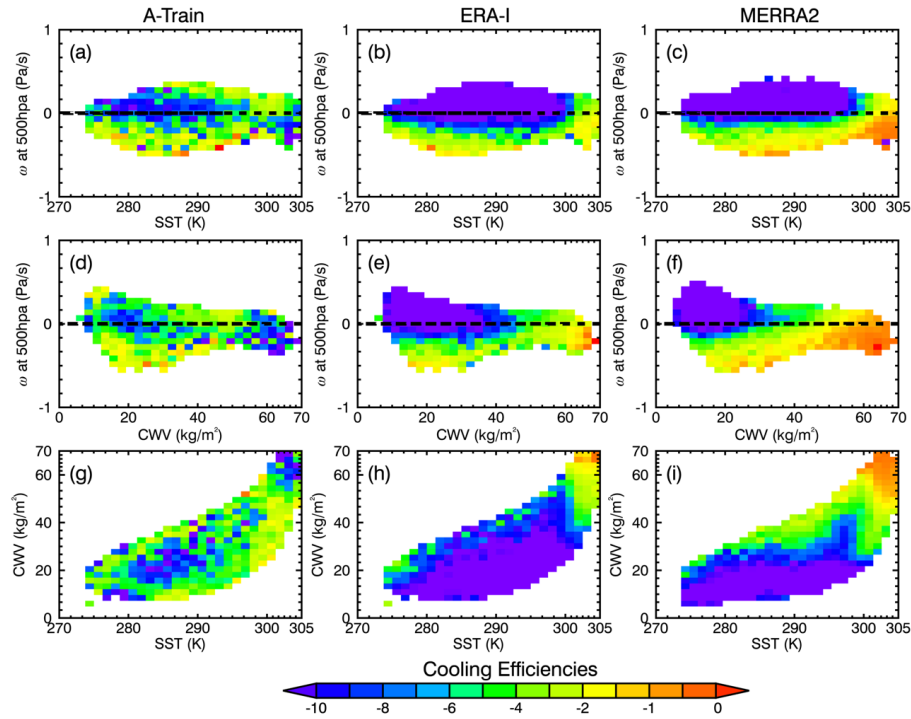
1127

1128

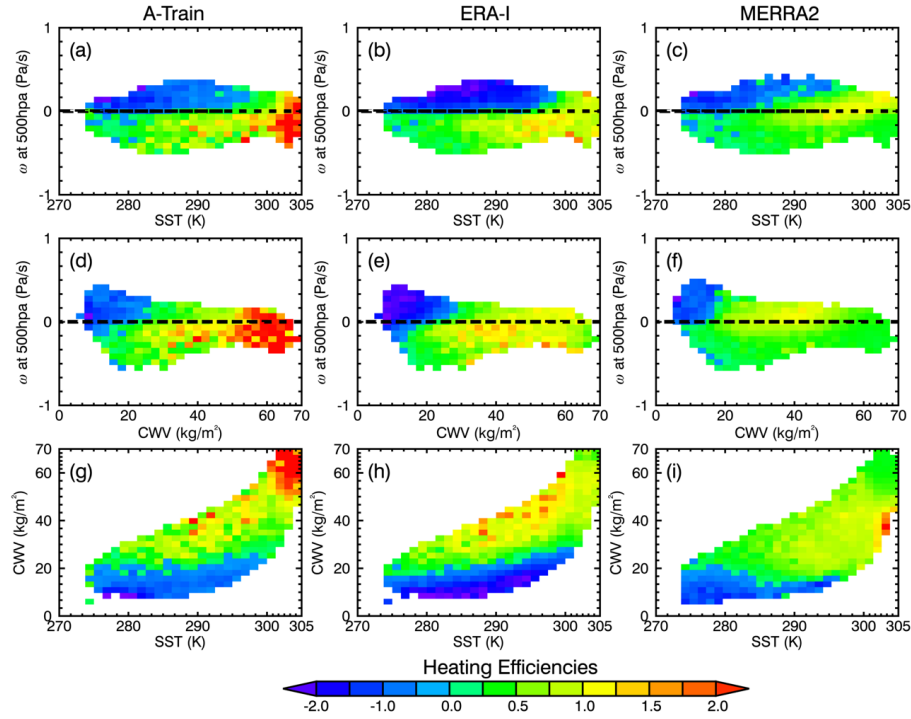
1129

1130

Figure 4: Distribution of the sample sizes at each bin corresponding to Figure 3. The blue line is the distribution of the sample sizes at each bin for MERRA-2 and the green line is A-Train and ERA-Interim. One should be noticed that A-Train and reanalysis have the same sample sizes as the ERA-Interim (green line) because all the R_c and R_h of A-Train have been matched with the environmental variables from ERA-Interim. R_c and R_h as a function of SST(a), CWV(b), and ω_{500} (c) obviously has the same sample size distributions.

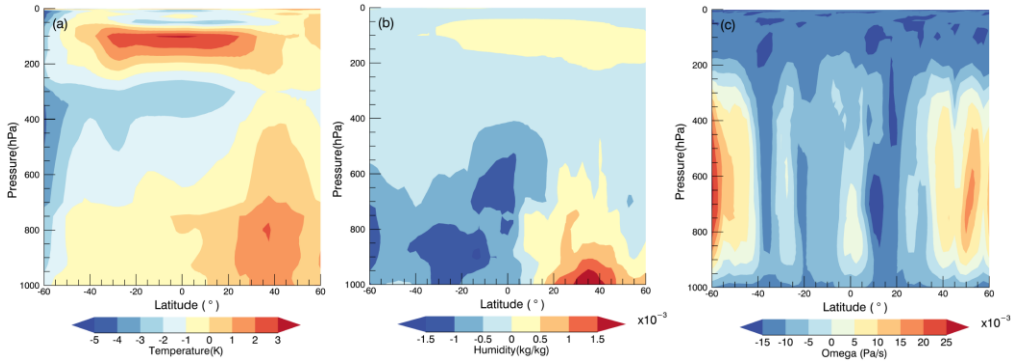


1131
 1132 **Figure 45:** Joint distributions of mean R_c derived from [CloudSat/A-Train](#)/ERA-
 1133 Interim/MERRA2 as a function of (a-c) SST vs ω_{500} , (d-f) CWV vs ω_{500} , (g-i) SST vs CWV from
 1134 ERA-Interim
 1135



1136
1137 **Figure 56:** All the same as Figure 54 but for R_h

1138
1139



1140

1141 **Figure 7:** Zonal mean difference of the vertical profiles of (a) air temperature, (b) specific
1142 humidity, and (c) ω between ERA-Interim and MERRA-2 matching the A-Train samples

1143 | between 2006-2010.

1144